

# COMPLEX ATTOSECOND TRANSIENT-ABSORPTION SPECTROSCOPY

DISSERTATION

Presented in Partial Fulfillment of the Requirements for the Degree Doctor of  
Philosophy in the Graduate School of The Ohio State University

By

Stephen J. Hageman, M.Sc.

Graduate Program in Physics

The Ohio State University

2019

Dissertation Committee:

Louis F. DiMauro, Advisor

Douglass Schumacher

Jay Gupta

Lawrence Robert Baker

© Copyright by  
Stephen J. Hageman  
2019

# ABSTRACT



## ACKNOWLEDGMENTS

# VITA

June 2011 .....	Bachelors of Science in Physics and Mathematics, Johns Hopkins University
Dec 2014 .....	Master of Science in Physics, The Ohio State University

## Publications

Antoine Camper, Hyunwook Park, **Stephen J. Hageman**, Greg Smith, Thierry Auguste, Pierre Agostini, and Louis F. DiMauro. High relative-phase precision beam duplicator for mid-infrared femtosecond pulses. Optics Letters, 44(22):5465-5468, November 2019.

B. Peters, A. Alfonsov, C. G. F. Blum, **S. J. Hageman**, P. M. Woodward, S. Wurmehl, B. Büchner, and F. Y. Yang, "Epitaxial films of Heusler compound  $\text{Co}_2\text{FeAl}_{0.5}\text{Si}_{0.5}$  with high crystalline quality grown by off-axis sputtering," Appl. Phys. Lett. 103, 162404 (2013)

W. G. Wang, A. Pearse, M. Li, **S. Hageman**, A. X. Chen, F. Q. Zhu, and C. L. Chien, "Parallel fabrication of magnetic tunnel junction nanopillars by nanosphere lithography," Scientific Report 3, 1948 (2013)

W. G. Wang, M. Li, **S. Hageman**, and C. L. Chien, "Electric-field-assisted switching in magnetic tunnel junctions," Nature Mater. 11, 64 (2012)

W. G. Wang, **S. Hageman**, M. Li, S. X. Huang, X. M. Kou, X. Fan, J. Q. Xiao, and C. L. Chien, "Thermal annealing study of magnetoresistance and perpendicular anisotropy in magnetic tunnel junctions based on MgO and CoFeB," Appl. Phys. Lett. 99, 102502 (2011)

# Table of Contents

	Page
Abstract . . . . .	ii
Dedication . . . . .	iii
Acknowledgments . . . . .	iv
Vita . . . . .	v
<b>List of Figures . . . . .</b>	<b>viii</b>
<b>List of Tables . . . . .</b>	<b>xiii</b>
 <b>Chapters</b>	
<b>1 Outline</b>	<b>1</b>
<b>2 Introduction</b>	<b>3</b>
2.1 HHG and APT . . . . .	3
2.2 CATS: real and imaginary . . . . .	3
<b>3 Design and construction of experimental apparatus</b>	<b>4</b>
3.1 Introduction . . . . .	4
3.2 Beamline . . . . .	4
3.2.1 Time Delay Control . . . . .	4
3.2.2 IR Dressing Intensity . . . . .	7
3.2.3 Spatial and Temporal Overlap . . . . .	10
3.2.4 Gas Sources for HHG . . . . .	10
3.3 Photon Spectrometer . . . . .	10
3.3.1 Spectrometer Calibration . . . . .	10
<b>4 Two-source high harmonic generation</b>	<b>12</b>
4.1 Introduction . . . . .	12
4.2 Theory . . . . .	12
4.2.1 Laser beam shaping using diffractive optics . . . . .	12
4.2.2 Beam splitting phase grating . . . . .	16
4.2.3 Square-wave phase grating design for high-harmonic generation . . . . .	22
4.3 Two-source high-harmonic generation . . . . .	27
4.4 Conclusion . . . . .	32
<b>5 Two-source refractive index measurement</b>	<b>34</b>

5.1	Introduction . . . . .	34
5.2	Complex refractive index . . . . .	34
5.3	Measurement of the complex refractive index . . . . .	36
5.3.1	Experimental setup . . . . .	36
5.3.2	Results . . . . .	38
5.4	Conclusion . . . . .	43
<b>6</b>	<b>Attosecond Transient-absorption Spectroscopy</b>	<b>44</b>
6.1	Introduction . . . . .	44
6.2	Theory . . . . .	44
6.3	Autoionization resonances . . . . .	44
6.3.1	Time-independent autoionization: Fano's original work . . . . .	44
6.3.2	Time-dependent autoionization . . . . .	51
6.3.3	Dipole Control Model . . . . .	52
6.4	Strong-field Transient Absorption in Argon . . . . .	52
6.4.1	Experimental setup . . . . .	52
6.4.2	Results . . . . .	52
6.5	Conculsion . . . . .	52
<b>7</b>	<b>Complex Attosecond Transient-absorption Spectroscopy</b>	<b>58</b>
7.1	Introduction . . . . .	58
7.2	Theory . . . . .	58
7.3	Complex Attosecond Transient-absorption Spectroscopy of Fano resonances . . . . .	58
7.3.1	Experimental setup . . . . .	58
7.3.2	Results . . . . .	58
7.4	Conculsion . . . . .	58
<b>8</b>	<b>Conclusion</b>	<b>59</b>
<b>Appendix A</b>	<b>Square-Wave Phase Grating</b>	<b>60</b>
<b>Bibliography</b>		<b>63</b>

# List of Figures

Figure	Page
3.1 Schematic of the beam path for the TABLE interferometer. The input laser is shown in red, its second harmonic in blue, and the generated XUV in purple. <b>BS</b> : Beamsplitter (Thorlabs BSF20-C), <b>I<sub>1</sub></b> and <b>I<sub>2</sub></b> : Irises used for alignment into interferometer. <b>DW</b> : Delay wedges for fine delay control, see section 3.2.1. <b>CF</b> : Color filter to remove parasitic colors from TOPAS (Thorlabs FELH1000). <b>HWP</b> : Half-wave plate. <b>WGP</b> : Wire grid polarizer. <b>RR</b> : Retro reflector for coarse delay adjustment. <b>FM</b> : Flip mirror. <b>TC</b> : Thermal camera used for alignment. <b>L<sub>1</sub></b> : $f = -300$ mm lens (Thorlabs LF1015-C). <b>L<sub>2</sub></b> : $f = 500$ mm lens (Thorlabs LA1380-C). <b>VW</b> : Vacuum window, 3 mm CaF <sub>2</sub> , <b>HM</b> : Hole mirror with 10 mm hole. <b>L<sub>3</sub></b> : $f = -400$ mm lens. <b>L<sub>4</sub></b> : $f = 500$ mm lens. <b>SWPG</b> : Square-wave phase grating. <b>L<sub>5</sub></b> : $f = 400$ mm lens. <b>BBO</b> : Second-harmonic generation crystal. <b>Cal</b> : Calcite. <b>GS</b> : Gas source for HHG. <b>MF</b> : Metallic filter. <b>EM</b> : Ellipsoidal mirror. <b>GC/SS</b> : Gas cell or solid sample. <b>RM</b> : Removable mirror for <i>in-situ</i> diagnostics. <b>ICC</b> : camera for <i>in-situ</i> diagnostics. <b>DG</b> : VLS diffraction grating. <b>BB</b> : Baffles to block zero order diffraction. <b>MCP/P</b> : Microchannel plate and phosphor. <b>AC</b> : Andor Neo 5.5 CMOS camera.	5
3.2 Schematic of the FS wedges used to control the time delay between the IR and XUV pulses in the dressing and generation arms interferometer, respectively. The wedges are aligned such that the input beam is normal to the first wedge face, and the beam exits the wedges normal to the last face of the second wedge. Only one of the wedges is motorized and is shown before and after a displacement by an amount $\Delta x$ .	6
3.3 Optical layout of the dressing arm of the TABLE interferometer. HWP and WGP are used to finely control the power in the dressing arm. The lenses L <sub>1</sub> and L <sub>2</sub> were chosen to achieve a high intensity at the focal plane in the target chamber. This was done to have the capability to drive strong-field processes in a gas medium [1]. See figure 3.1 for full details of the interferometer.	8

3.4	(a) Beam profile of the signal from the TOPAS pumped by the Spitfire laser system. Wavelength is 1430 nm and the pulse is normalized to 1 $\mu\text{J}$ of pulse energy. Beam profile was measured using a thermal camera, and is used as the input to the beam propagation simulation that is initiated just before L <sub>1</sub> in figure 3.3. (b) Numerically propagated beam profile just after L <sub>2</sub> in figure 3.3. (c) Beam profile just after reflecting off the hole mirror. (d) Calculated intensity profile at the focal plane in the interaction region. (e) Lineout of the calculated intensity profile. For an input pulse energy of 1 $\mu\text{J}$ , a peak intensity of 0.33 TW/cm <sup>2</sup> can be achieved. (f) Integrated average power at different point in the calculation. The main source of energy loss is due to the hole mirror, which only reflects 52% of the incident light. The hole mirror has an inner radius of 5 mm in this case. . . . .	9
3.5	INCOMPLETE: Autocorrelation to find temporal overlap. . . . .	11
3.6	INCOMPLETE: HPGC filament . . . . .	11
4.1	Schematic demonstrating how to use a diffractive optical element to shape the beam profile at the focal plane. A collimated coherent beam is incident upon a diffractive optical element which shapes the phase of the incident beam, and then a lens is used as a transform element to Fourier transform the beam at the focal plane. The intensity profile at the focal plane can be controlled by altering the spatial dependence of the phase imparted upon the incident beam by the phase element. Adapted from [2] . . . . .	13
4.2	Plot of the phase function $\phi(x - x_0)$ in units of $\pi$ for a $0 - \pi$ SWPG with a period of $d$ . The dark blue (light blue) curve shows the phase function for $x_0 = 0$ ( $x_0 = d/10$ ). . . . .	17
4.3	Square complex modulus of the Fourier coefficients $a_n$ of the $0 - \pi$ SWPG. The square complex modulus is proportional to the energy put into each diffraction order. As can be seen from figure, the $\pm 1$ orders have the most energy put into them at $4/\pi^2 \approx 41.1\%$ each. All even orders have zero energy. . . . .	19
4.4	Intensity profile $S(\tilde{x})$ at the focal plane. Horizontal units are scaled by the spacing between orders, $\tilde{x}_1 = \lambda f/d$ . Phase is also plotted for two different offset positions $x_0 = d/3$ and $x_0 = d/5$ . This demonstrates the ability of the SWPG to generate two sources and control the relative phase between them. Calculated by numerically propagating the beam profile and SWPG in figure 4.5. . . . .	20
4.5	(a) Intensity profile of the input beam measured by a thermal camera. (b) Phase imparted by $0 - \pi$ SWPG with a grating period of $d = 2.5$ mm. . . . .	20
4.6	Square complex modulus of the Fourier coefficients $a_n$ of the $0 - \zeta\pi$ SWPG for several values of $\zeta$ . The square complex modulus is proportional to the energy put into each diffraction order. As can be seen from figure, the $\pm 1$ orders have the most energy put into them even for $\zeta \neq 1$ . All non-zero even orders have zero energy. . . . .	22
4.7	Pulse energy output of the TOPAS used in the experiments described within this chapter. The optimal output energy of the TOPAS can be seen to be around 1350 nm. This is the wavelength that was selected as the design wavelength for the SWPG. . . . .	23

4.8	Refractive index (blue curve and axis) and the $\zeta$ parameter (red curve and axis). For a 70 nm bandwidth pulse centered at 1350 nm, $\zeta - 1$ varies from -0.026 to 0.027 assuming normal incidence. . . . .	24
4.9	Non- $\pi$ phase step parameter $\zeta(\lambda, \theta)$ calculated for a range of relevant wavelengths and incident angles. The ability to effectively tune the optical path length of the step enables the SWPG to be used for a much larger range of wavelengths that are longer than the initial design wavelength. . . . .	25
4.10	Calculation of intensity at the focal plane of the SWPG for various parameters of $\beta$ . Calculation is done my numerically propagating the measured beam profile shown in 4.5. $\beta$ is varied by adjusting the radius of the input beam profile. As $\beta \rightarrow 0$ , one can see that the performance of the SWPG deteriorates and not longer produces well separated sources. . . . .	25
4.11	Schematic of the two SWPG which were purchased from Silios. They are constructed by etching the phase step in Corning HPFS 7980 fused-silica. . . . .	26
4.12	Schematic of the two-source HHG experiment performed in the TABLE. A $0 - \pi$ SWPG is used to generate two intense lobes at the focus of a lens. These lobes will generate XUV beams which will interfere in the far-field. An ellipsoidal mirror is used to refocus the XUV beams before going onto the spectrometer. . . . .	27
4.13	False color image of the two sources from the SWPG driving ionization in a gas medium delivered by the piezo gas jet shown in the image. Two sources follow the red arrows, and the XUV that is generated is shown by blue arrows. . . . .	28
4.14	(a) Reference harmonic spectrum generated with a $0 - \pi$ SWPG. The fringes along the sensor position dimension are due to interference between the two XUV sources that are generated. The position of the fringe pattern is determined by the relative phase between the two sources. This relative phase can be controlled by the SWPG. (b) Power spectrum of the Fourier transform of the above image along the sensor position dimension. Clear peaks can be seen corresponding to the spatial frequency for each harmonic order. The linear dependence of the spatial frequency on photon energy is also seen. . . . .	29
4.15	(a) Reference harmonic spectrum with dots showing the harmonic orders whose spatialgrams are plotted below. (b)-(e) Spatialgrams for harmonic orders 29, 33, 39, and 45. Tilted fringe pattern shows fringe shift due to phase shift induced by translating the phase grating. Modulations with a period od $d/2$ arise because of interference between the two generating sources. . . . .	30
4.16	(a) Spatialgram of all harmonic orders combined. Diagonal stripes show the attosecond pulses that make up the APT. (b) Lineout from the full spatialgram. . . . .	32
4.17	(a) Spatialgram of all harmonic orders combined. Diagonal stripes show the attosecond pulses that make up the APT. A second harmonic field was added to break the symmetry and generate even harmonics. (b) Lineout from the full spatialgram. Only two attosecond bursts are seen, which is expected from the asymmetric two-color generation field. The increased modulation with a period $d/2$ is due to the stronger interference between the two sources. . . . .	33

5.1	Schematic of the real part of the refractive index versus photon energy. Example resonances are shown in the IR, the visible/UV, and in the XUV/soft x-ray regimes. In general, the refractive index approaches 1 at higher photon energies. Adapted from [3]. . . . .	35
5.2	Schematic of a Mach-Zehnder interferometer that is used to measure the phase shift induced by a sample placed in one of the arms of the interferometer. For the experiments described in this chapter, the two XUV sources will act as the two arms of a Mach-Zehnder. Modified from [3]. . . . .	37
5.3	Schematic of the two-source HHG experiment performed in the TABLe. A $0 - \pi$ SWPG is used to generate two intense lobes at the focus of a lens. These lobes will generate XUV beams which will interfere in the far-field. An ellipsoidal mirror is used to refocus the XUV beams into a target chamber before going onto the spectrometer. A sample that is shaped like a step-function will be introduced at the focus of the XUV in the target chamber. The spatial profile of the various harmonic orders will be measured in the two cases shown. The fringe shift and fringe contrast changes allow for a simultaneous measurement of both parts of the refractive index of the sample.	37
5.4	Schematic of the sample that was used in this experiment. It is a free standing 260 nm Si membrane that has been broken in half. The way that the sample was cleaved in half ensures that the edge is sharper than the separation between the two sources. The sample was made by Norcada before it was broken. . . . .	39
5.5	(a) Spatial profile of harmonic order 29 as the silicon sample is translated through the two sources. Three regimes are clear from the spatial profile, and they correspond to both sources going through vacuum, only one source going through the sample, and both sources going through the sample. A clear fringe shift can be seen between the second regime and the other two. Additional structure is seen at the transition between regimes, and this is due to diffraction caused by the sample partially blocking one of the sources. (b) Phase extracted from the spatial frequency corresponding to this harmonic order. The phase shift induced by the Si sample can be extracted from this phase shift. . . . .	40
5.6	(a) Spatial profile of harmonic order 29 as the silicon sample is translated through the two sources. Three regimes are clear from the spatial profile, and they correspond to both sources going through vacuum, only one source going through the sample, and both sources going through the sample. (b) Fringe contrast extracted from the spatial frequency corresponding to this harmonic order. . . . .	41
5.7	(a) Real part of the refractive index measured using a SWPG. Shows excellent agreement with the values from CXRO. (b) Imaginary part of the refractive index measured using a SWPG. Shows excellent agreement with the values obtained from CXRO. . . . .	42

6.1	Level diagram of argon showing the effect of autionization states on XUV photoabsorption. There are two possible pathways for ionization with a photon of energy $\Omega$ : (1) direct ionization to a continuum state (left side of figure) and (2) excitation to a bound state in the continuum (right side of figure). In case (2), there is coupling between the bound state and the continuum through the configuration interaction. This allows for the bound state to decay to the same continuum state as in case (1). These effect leads to interference between these two pathways. . . . .	45
6.2	(a) Calculation of the photoabsorption cross section near a resonance for the listed $q$ parameters. The change from symmetric to asymmetric profiles can be seen as the $q$ parameter is varied. Maximum and minimum in cross section occurs at $\epsilon = 1/q$ and $\epsilon = -q\Gamma^2/4$ , respectively. (b) Calculation of the phase across the resonance for different $q$ parameter. The $\pi$ phase jump clearly depends on $q$ , and it occurs when $\epsilon = -q$ and not at the resonance energy $E_r$ . Calculations based on U. Fano's original work [4]. . . . .	50
6.3	Photoabsorption cross section of the Argon $3s3p^6np$ Fano resonances (blue curve), with only resonances up to $n = 8$ shown. Grey shaded area indicates the energetic region above the $\text{Ar}^+(3s3p^6)$ ionization threshold. Values used to calculate this cross section are shown in Table 6.1. . . . .	50
6.4	Incomplete . . . . .	53
6.5	Incomplete . . . . .	53
6.6	Incomplete . . . . .	54
6.7	$\varphi_1 = 0$ . . . . .	55
6.8	$\phi_0 = 4p$ $a_1 = 0$ , $\phi_1 = 0$ , $a_1 = 0.8$ , $\phi_1 = \pi/2$ . . . . .	56
6.9	$\phi_0 = 4p$ $a_1 = 0$ , $\phi_1 = 0$ , $a_1 = 0.8$ , $\phi_1 = \pi/2$ . . . . .	57
6.10	Incomplete . . . . .	57
A.1	Camera image of two sources generating a filament in a gas cell. Image was taken while chamber was vented and at ambient pressure. . . . .	61
A.2	Camera image of the output of the phosphor screen. Harmonics are visible by eye. . . . .	62

# List of Tables

Table	Page
6.1 Paramters of the $3s3p^6np$ Fano resonances in argon. These values were extracted from experimental cross sections, see [5–7]. . . . .	49

# Chapter 1

## OUTLINE

### 1. Introduction

- Brief introduction to HHG and APT
- Introduce general theory of transient absorption and motivate measuring both real and imaginary parts of the dipole/refractive index

### 2. Beamline Design and construction

- Briefly introduce overall beamline
- Spectrometer design
  - VLS grating theory and flat-field calculations
  - Chamber and detector design

### 3. Phase Grating

- Introduce general beam shaping problem
- SWPG design for HHG
- Non- $\pi$  SWPG
- Two-source HHG
  - Relative phase control by scanning grating
  - Two-source interference effects
  - Interferometric autocorrelation
- Spectrometer calibration using SWPG and spectral features

### 4. Refractive Index Measurement

- Introduce complex refractive index
- Experimental setup and sample design

- Measurement of refractive index by fringe shift and contrast
- Comparison to CXRO and literature

5. One-source Transient Absorption

- Transient absorption theory
- Argon Fano resonances
- Strong-field transient absorption of argon

6. Two-source Transient Absorption

- Experimental setup
- Demonstrate measuring real and imaginary parts using fringe shift and contrast

# **Chapter 2**

## **INTRODUCTION**

**2.1 HHG and APT**

**2.2 CATS: real and imaginary**

# Chapter 3

## DESIGN AND CONSTRUCTION OF EXPERIMENTAL APPARATUS

### 3.1 Introduction

### 3.2 Beamline

#### 3.2.1 Time Delay Control

An important consideration in pump/probe experiments is how to control the delay between the pump and probe pulses. To control this delay, there are typically two methods that can be employed optically. The first to use a retro-reflector that is mounted on a motorized stage [8–13]. With this method, the delay is simply related to the displacement of the motorized stage by the relationship  $\Delta\tau = 2\Delta x/c$ . This means that a displacement of 10 nm by the motorized stage would lead to a delay of 67 as, whereas a displacement of 2 in. would lead to a delay of 339 ps. This setup is advantageous if large delays are required (10s of ps to a few ns), however for the short time steps that are required for an attosecond measurement (typically on the order of 100 as) the requirements on the motor being used to move the retro are very high. Since a 100 as step would equate to a translation of 15nm, this would require the use of a piezoelectric motor. Piezo motors and their associated electronics tend to be expensive, and they have inherent problems because they exhibit nonlinear movement due to hysteresis and they tend to drift and creep after actuation. This can be abated through a feedback sensor and operating it in a closed-loop mode, however the quality of the sensor and electronics determines how effectively these problems are minimized.

The second common method to control the delay between the pump and probe pulse is to use a pair of glass wedges [1, 14, 15]. A schematic of how this is achieved is shown in figure 3.2. In this scheme, only one of the glass wedges is motorized, and the direction of translation is perpendicular to the input beam and parallel to the first glass face. The path that a ray would take through the wedge pair is shown before ( $a \rightarrow b \rightarrow c$ ) and after ( $a' \rightarrow b' \rightarrow c'$ ) translation by an amount  $\Delta x$ . Assuming that the wedge angle is  $\theta$ , the path

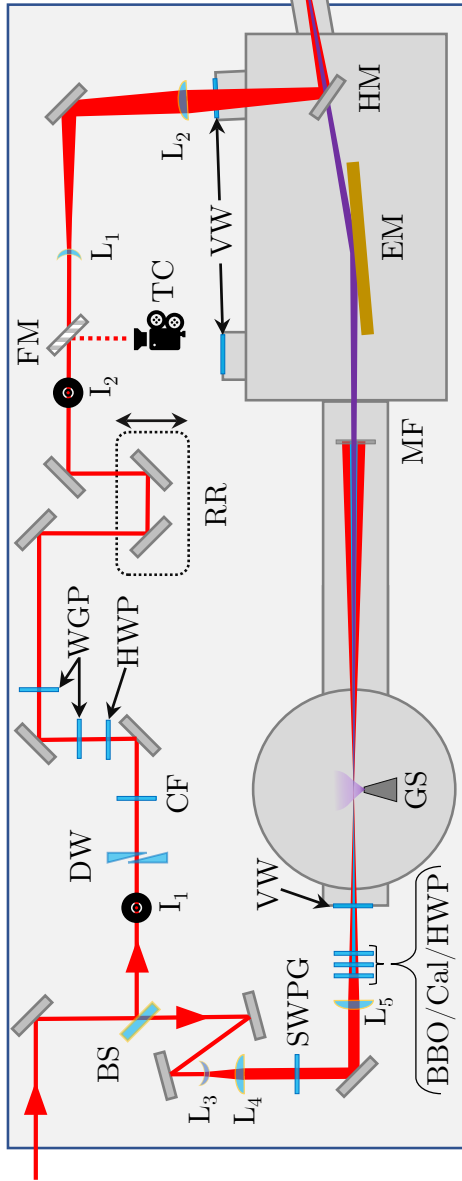


Figure 3.1: Schematic of the beam path for the TABLe interferometer. The input laser is shown in red, its second harmonic in blue, and the generated XUV in purple. **BS**: Beamsplitter (Thorlabs BSF20-C). **I<sub>1</sub>** and **I<sub>2</sub>**: Irises used for alignment into interferometer. **DW**: Delay wedges for fine delay control, see section 3.2.1. **CF**: Color filter to remove parasitic colors from TOPAS (Thorlabs FELH1000). **HWP**: Half-wave plate. **WGP**: Wire grid polarizer. **RR**: Retro reflector for coarse delay adjustment. **FM**: Flip mirror. **TC**: Thermal camera used for alignment. **L<sub>1</sub>**:  $f = -300$  mm lens (Thorlabs LF1015-C). **L<sub>2</sub>**:  $f = 500$  mm lens (Thorlabs LA1380-C). **VW**: Vacuum window, 3 mm CaF<sub>2</sub>, **HM**: Hole mirror with 10 mm hole. **L<sub>3</sub>**:  $f = -400$  mm lens. **L<sub>4</sub>**:  $f = 500$  mm lens. **SWPG**: Square-wave phase grating. **L<sub>5</sub>**:  $f = 400$  mm lens. **BBO**: Second-harmonic generation crystal. **CaI**: Calcite. **GS**: Gas source for HHG. **MF**: Metallic filter. **EM**: Ellipsoidal mirror. **GC/SS**: Gas cell or solid sample. **RM**: Removable mirror for *in-situ* diagnostics. **ICC**: camera for *in-situ* diagnostics. **DG**: VLS diffraction grating. **BB**: Baffles to block zero order diffraction. **MCP/P**: Microchannel plate and phosphor. **AC**: Andor Neo 5.5 CMOS camera.

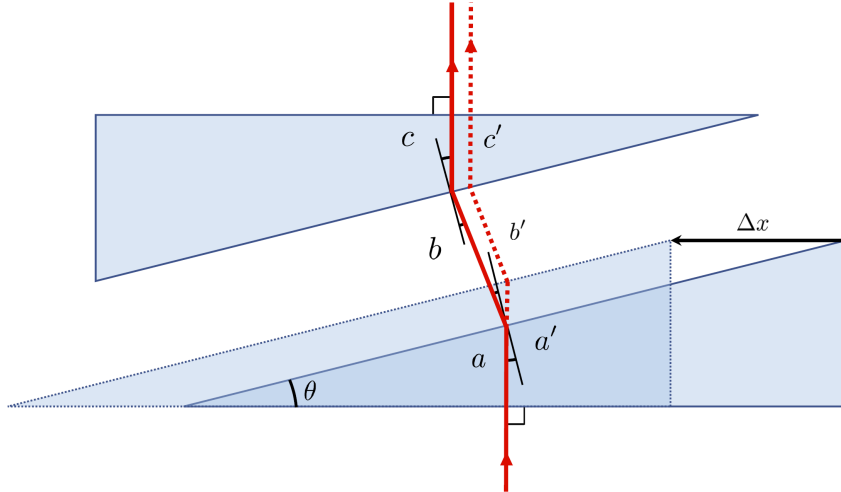


Figure 3.2: Schematic of the FS wedges used to control the time delay between the IR and XUV pulses in the dressing and generation arms interferometer, respectively. The wedges are aligned such that the input beam is normal to the first wedge face, and the beam exits the wedges normal to the last face of the second wedge. Only one of the wedges is motorized and is shown before and after a displacement by an amount  $\Delta x$ .

after translation by  $\Delta x$  can be written as

$$a' = a + \Delta x \tan \theta \quad (3.1)$$

$$b' = b - \Delta x \left( \frac{\sin \theta}{\cos \psi} \right) \quad (3.2)$$

$$c' = c - \Delta x \tan \theta \sin \theta \frac{\cos(\frac{\pi}{4} + \psi)}{\sin(\frac{\pi}{4} + \theta + \psi)} \quad (3.3)$$

where

$$\psi = \arcsin(n \sin \theta) \quad (3.4)$$

is given by Snell's Law [16]. From the difference in optical path length between these two paths, one can calculate the time delay  $\Delta\tau$  introduced by a translation of  $\Delta x$ , and this relationship is given by

$$\Delta\tau = \frac{\Delta x}{c} \left[ (n-1) \tan \theta - \frac{\sin \theta}{\cos \psi} - (n-1) \tan \theta \sin \theta \left( \frac{\cos(\frac{\pi}{4} + \psi)}{\sin(\frac{\pi}{4} + \theta + \psi)} \right) \right]. \quad (3.5)$$

For a pair wedges made out of fused silica with a wedge angle of  $\theta = 5^\circ$  and a beam of wavelength 1430 nm, equation 3.5 becomes

$$\Delta\tau = \left( 101 \left[ \frac{\text{as}}{\mu\text{m}} \right] \right) \Delta x. \quad (3.6)$$

This entails that a translation of  $1 \mu\text{m}$  would lead to a delay of only 100 as. This reduction in motor step to delay step ratio compared to the retroreflector case means that the requirements on the motorized stage are greatly reduced. Additionally, since the glass wedges are a transmissive optic, they are inherently less sensitive to vibrations when compared to a retroreflector.

In the TABLE apparatus, both types of delay control have been implemented, as shown in figure 3.1. The retroreflector is mounted on a translation stage with 2 inches of travel that is controlled manually with a micrometer. The primary use for the retroreflector is to make coarse adjustments to the dressing arm to account for changes in temporal overlap between the two arms of the interferometer. Typically, this is due to adjustments made to the interferometer itself (such as introducing new optics) or due to changes in the input laser, usually either pointing or wavelength.

To finely control the delay, a pair of glass wedges is used. These wedges are made out of fused silica, and have a wedge angle of  $\theta = 5^\circ$ . The first of the two wedges are motorized in manner similar to that shown in figure 3.2. The stage that the first wedge is mounted to has a total travel of 1 inch, and it is controlled by a Thorlabs Z825B DC servo motor. This "pencil" motor, as it is known in the lab, has a minimum repeatable incremental motion of  $0.2 \mu\text{m}$  and is encoded, so its absolute position is known to within the homing accuracy of  $\pm 1 \mu\text{m}$ . From equation 3.6, using these wedges at 1430 nm with a step size of  $1 \mu\text{m}$  will give a delay of 101 as.

### 3.2.2 IR Dressing Intensity

An important consideration in any ATS experiment is the intensity of the IR field that is used as a probe/dressing field. Ideally, one would like to be able to control the intensity such that both perturbative and strong-field regimes can be accessed with the same optical setup. This can be achieved by selecting an optical setup that has a high peak intensity and then attenuate the beam to achieve a lower intensity. Attenuation can be achieved through the use of neutral density (ND) filters, however they can lead to several complications. Since the ND filter would be placed in only one arm of the interferometer to control only the dressing intensity, any variation in thickness between different ND filters would lead to a change in temporal overlap. Additionally, any change in positioning when switching ND filters will lead to a slight change in spatial overlap. In light of this, the method to attenuate the beam that was implemented in the TABLE interferometer is a half-wave plate (HWP) and a wire grid polarizer (WGP). By rotating the polarization using the HWP, we can finely control the intensity of the dressing field by using the WGP to transmit only one component of the rotated polarization. The WGP is set such that the initial polarization is maintained, and this insures that the polarization of the IR and XUV are parallel in the interaction region. A second WGP is used to increase the effective extinction ratio to

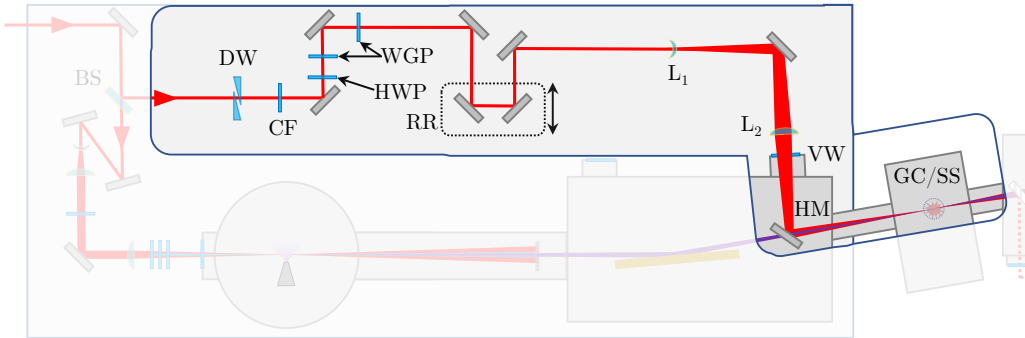


Figure 3.3: Optical layout of the dressing arm of the TABLE interferometer. HWP and WGP are used to finely control the power in the dressing arm. The lenses  $L_1$  and  $L_2$  were chosen to achieve a high intensity at the focal plane in the target chamber. This was done to have the capability to drive strong-field processes in a gas medium [1]. See figure 3.1 for full details of the interferometer.

ensure that the field is linearly polarized even when it is being strongly attenuated. The extinction ratio of one of the WGP (Thorlabs WP25M-UB) is approximately 12500:1 at 1430 nm. Using this setup in conjunction with a beam splitter that reflects 8% of the input energy to the dressing arm, the pulse energy can be tuned between 1  $\mu\text{J}$  and 125  $\mu\text{J}$ .

The next design consideration for the dressing arm of the interferometer is choosing focusing optics to set the peak intensity that is achievable at the interaction region. The two main options in this regard are either focusing mirrors or lenses. Focusing mirrors have a significant advantage in the fact that they are achromatic, however their use leads to an optical system that is generally larger in optical path length and is difficult to switch between focal geometries. Lenses in that regard are well suited to adjusting between different experimental requirements without changing the overall footprint of the interferometer. The dressing lenses that are used in all of the experiments in this dissertation are shown in 3.3, and they were originally selected to achieve the highest possible intensity at the focal plane given the geometrical constraints of the TABLE [1]. This choice of lenses was made to drive strong-field processes in rare gas atoms in the interaction region, and they were selected based upon calculations done by D. Kiese wetter using a hole mirror as both beam splitters in the interferometer. His calculations estimated that the peak intensity at 1300 nm was 0.59 TW/cm<sup>2</sup> for a pulse energy of 1  $\mu\text{J}$  just before  $L_1$  in figure 3.3.

For the experiments described herein, the initial beam splitter was changed to a beam sampler and the recombining hole mirror was changed to a hole diameter of 10 mm from 6 mm. This was done to maximize the XUV flux by sending as much energy to generation as possible while minimizing clipping of the XUV with the hole mirror. In light of these changes, it is important to determine what the new peak intensity is at the focus. To

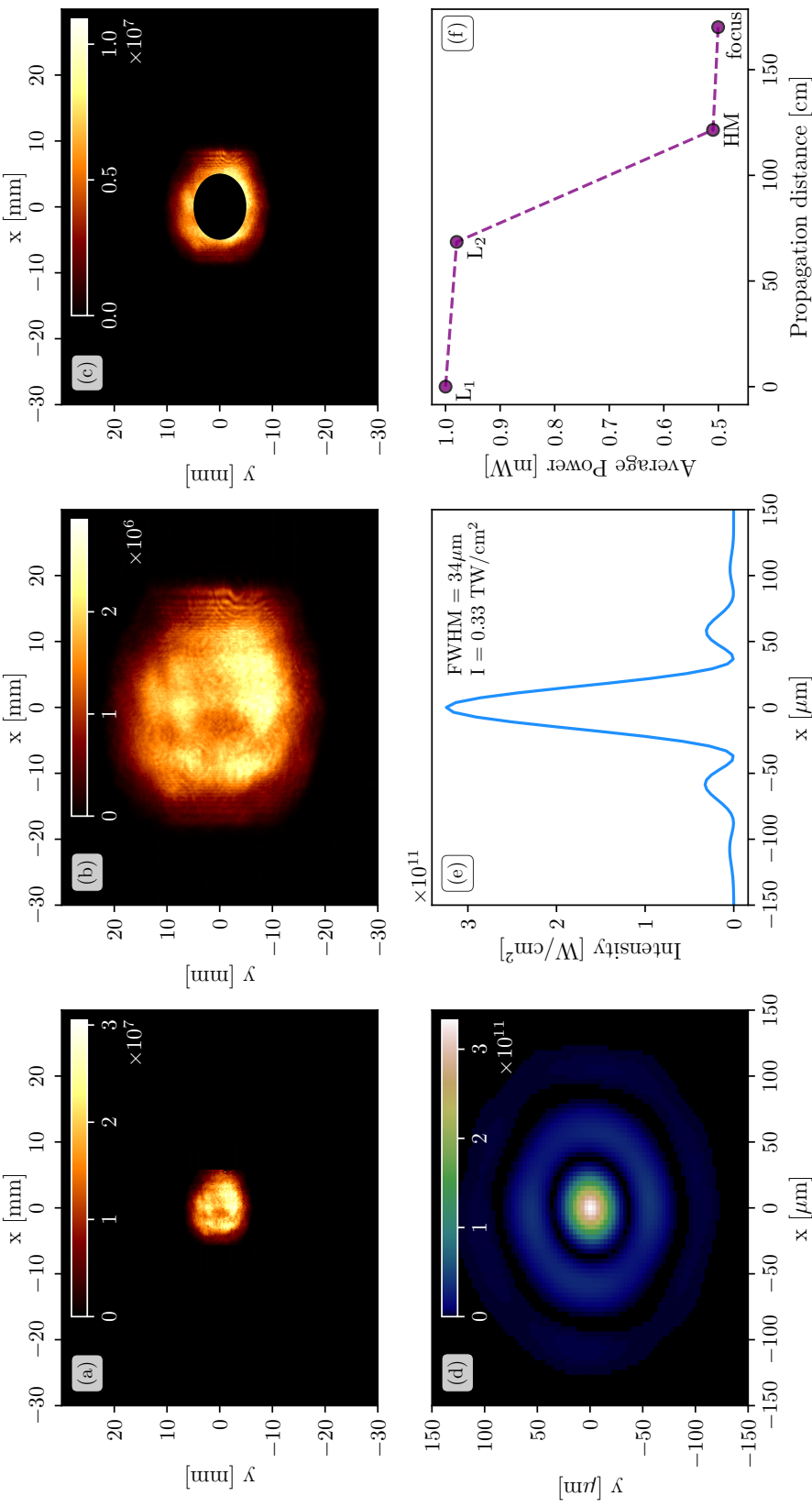


Figure 3.4: (a) Beam profile of the signal from the TOPAS pumped by the Spitfire laser system. Wavelength is 1430 nm and the pulse is normalized to 1  $\mu\text{J}$  of pulse energy. Beam profile was measured using a thermal camera, and is used as the input to the beam propagation simulation that is initiated just before L<sub>1</sub> in figure 3.3. (b) Numerically propagated beam profile just after L<sub>2</sub> in figure 3.3. (c) Beam profile just after reflecting off the hole mirror. (d) Calculated intensity profile at the focal plane in the interaction region. (e) Lineout of the calculated intensity profile. For an input pulse energy of 1  $\mu\text{J}$ , a peak intensity of 0.33 TW/cm<sup>2</sup> can be achieved. (f) Integrated average power at different point in the calculation. The main source of energy loss is due to the hole mirror, which only reflects 52% of the incident light. The hole mirror has an inner radius of 5 mm in this case.

accurately determine the intensity, a beam propagation simulation is performed using the measured beam profile. It is important to use the measured beam profile because the spatial mode out of the TOPAS is decidedly non-Gaussian, and this can be seen in 3.4 (a) which shows the beam profile at 1430 nm measured on a thermal camera. Beam propagation is implemented using an open-source Python package developed by Flexible Optical B.V. (OKO Tech) called LightPipes. The package consists of numerical methods to calculate the Fresnel integral

$$u(x, y, z) = \frac{ik}{2\pi z} e^{ikz} e^{ik(x^2+y^2)/2z} \int_{-\infty}^{\infty} \int_{-\infty}^{\infty} u(\xi, \eta, 0) e^{ik(\xi^2+\eta^2)/2z} e^{-ik(x\xi+y\eta)/z} d\xi d\eta \quad (3.7)$$

which gives the field  $u(x, y, z)$  after propagation of a distance  $z$ , given an initial field profile of  $u(x, y, 0)$ . Using this formalism, a thin lens of focal length can be treated as adding a quadratic phase  $\phi = -\pi(x^2 + y^2)/\lambda f$  to the field, and the effect of apertures can also be included to account for the effect of diffraction on the beam profile and intensity [17].

The results of the simulation are shown in figure 3.4. This simulation was performed for an input pulse energy of 1  $\mu$ J at a wavelength of 1430 nm. The simulation begins just before L<sub>1</sub> in 3.3 and the beam is propagated through to the interaction region GC/SS. The beam profile at L<sub>2</sub> and immediately after the hole mirror is shown in figure 3.4 (b) and (c), and the intensity profile at the focus is shown in figure 3.4 (d). From these simulations, the peak intensity for a pulse energy of 1  $\mu$ J is 0.33 TW/cm<sup>2</sup>. For the range of pulse energies available in the dressing arm, this corresponds to an intensity range of 0.33 - 413 TW/cm<sup>2</sup> that is achievable.

### 3.2.3 Spatial and Temporal Overlap

### 3.2.4 Gas Sources for HHG

## 3.3 Photon Spectrometer

### 3.3.1 Spectrometer Calibration

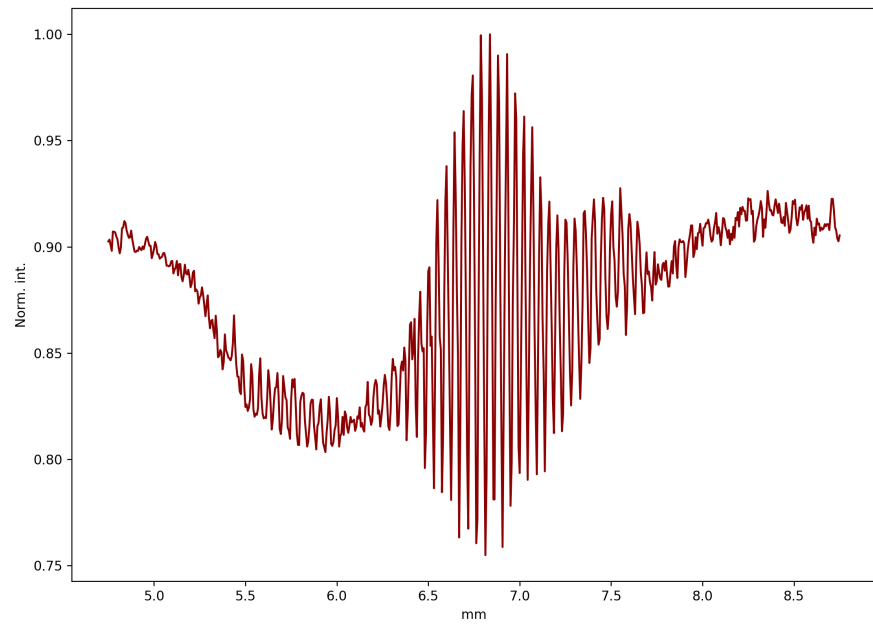


Figure 3.5: INCOMPLETE: Autocorrelation to find temporal overlap.

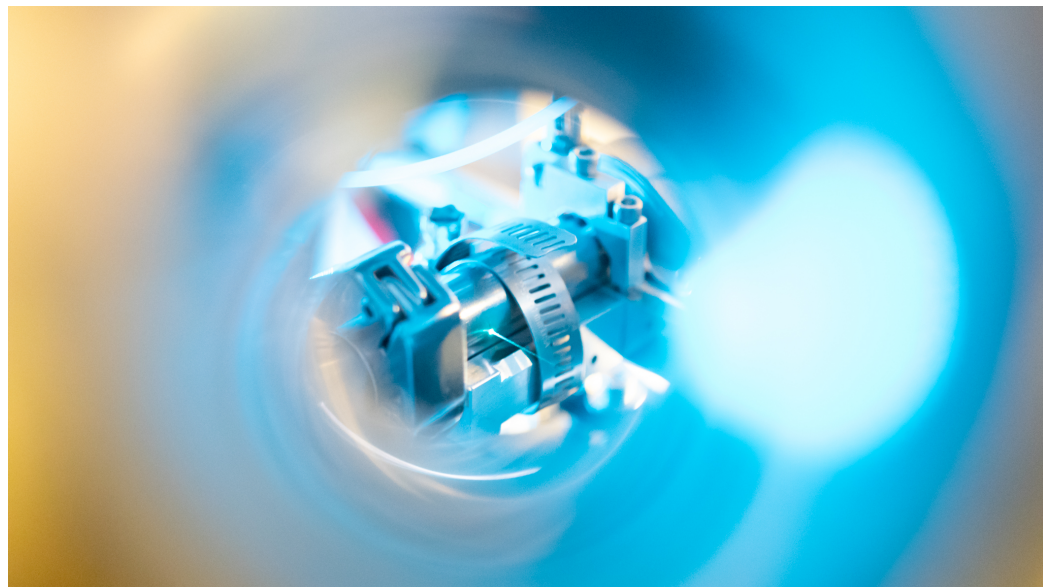


Figure 3.6: INCOMPLETE: HPGC filament

# Chapter 4

## TWO-SOURCE HIGH HARMONIC GENERATION

### 4.1 Introduction

A common difficulty in working with extreme ultraviolet (XUV) light is the lack of efficient and broadband optics, especially beam splitters. In this chapter, I will introduce a method for generating two sources of XUV light by high harmonic generation (HHG) using a square-wave phase grating (SWPG). This SWPG allows for the duplication of an infrared (IR) pulse, as well as precise and stable control of the relative phase between the duplicates of the input IR pulse. The two most intense duplicates can generate harmonics which will interfere in the far-field. This can be thought of as an inline Mach-Zehnder interferometer with interferometric stability on sub-wavelength level of the high harmonic. The inherent stability of this two-source scheme will be utilized to measure both the real and imaginary parts of the refractive index of a medium.

### 4.2 Theory

#### 4.2.1 Laser beam shaping using diffractive optics

In many experimental designs, it is advantageous to be able to shape the spatial intensity distribution of light to be something other than a typical Gaussian beam. A common example of this is generating a beam with an approximately constant intensity across its spatial profile (a flat-top beam). For the experiments described herein, we will be interested in duplicating an input beam with relative phase control between the two duplicate beams. Both of these examples are part of the general concept of laser beam shaping. The challenge is to design an optical system such that given an input beam profile  $I_{in}(x, y)$  we can generate the desired output beam profile  $I_{out}(x, y)$ . Ideally, this optical system is designed in such a way that it can be nearly lossless. The relevant optical system which will be discussed in this chapter is shown in figure 4.1. The system consists of a phase element which modifies

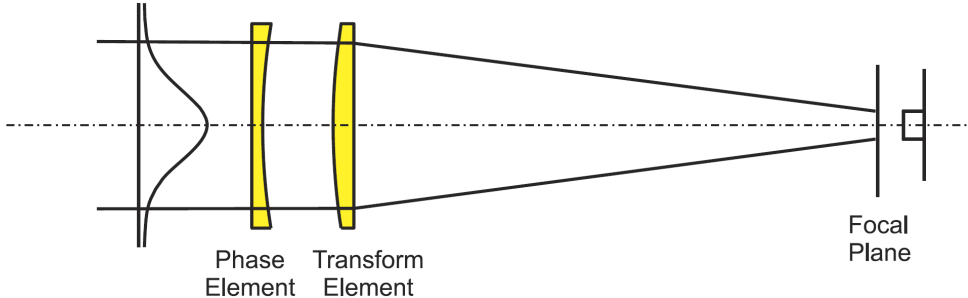


Figure 4.1: Schematic demonstrating how to use a diffractive optical element to shape the beam profile at the focal plane. A collimated coherent beam is incident upon a diffractive optical element which shapes the phase of the incident beam, and then a lens is used as a transform element to Fourier transform the beam at the focal plane. The intensity profile at the focal plane can be controlled by altering the spatial dependence of the phase imparted upon the incident beam by the phase element. Adapted from [2]

the phase of the input field by  $\phi(x, y)$  and a Fourier transform lens which adds a quadratic phase to the beam to focus it at the focal plane. By appropriate choice of the phase profile of the phase element, one can produce the desired beam profile at the focal plane.

This problem can be theoretically described in terms of Fourier optics [2, 17, 18]. If one assumes that a field  $u(x, y, 0)$  is incident upon an aperture at  $z = 0$ , then the field for  $z > 0$  can be written under the Fresnel approximation by the Fresnel integral

$$u(x, y, z) = \frac{ik}{2\pi z} e^{ikz} e^{ik(x^2+y^2)/2z} \int_{-\infty}^{\infty} \int_{-\infty}^{\infty} u(\xi, \eta, 0) e^{ik(\xi^2+\eta^2)/2z} e^{-ik(x\xi+y\eta)/z} d\xi d\eta \quad (4.1)$$

where  $u(\xi, \eta, 0)$  is the incoming field and  $k = 2\pi/\lambda$  is the wavenumber. Now, if one assumes that the phase element is placed at  $z = 0$ , then immediately after passing through the thin phase element in Fig. 4.1 the field is given by

$$u(\xi, \eta, 0) = f(\xi, \eta) e^{i\phi(\xi, \eta)}. \quad (4.2)$$

After propagating through the thin Fourier transform lens of focal length  $f$ , a phase of  $k(\xi^2\eta^2)/2f$  is added to the beam, and the field at the focal plane is now given by

$$u(x, y, f) = \frac{ik}{2\pi f} e^{ikf} e^{ik(x^2+y^2)/2f} \int_{-\infty}^{\infty} \int_{-\infty}^{\infty} f(\xi, \eta) e^{i\phi(\xi, \eta)} e^{-ik(x\xi+y\eta)/f} d\xi d\eta \quad (4.3)$$

where the quadratic phase in integral of equation 4.1 is exactly canceled by the quadratic phase introduced by the lens.

Now, the idea is to rewrite this field profile at the focal plane into a more intuitive form

by introducing the equation

$$g(\xi, \eta) = \frac{ik}{2\pi f} f(\xi, \eta) e^{i\psi(\xi, \eta)}. \quad (4.4)$$

The Fourier transform of this function  $g(\xi, \eta)$  is given by

$$G(a, b) = \frac{ik}{2\pi f} \int_{-\infty}^{\infty} \int_{-\infty}^{\infty} f(\xi, \eta) e^{i\psi(\xi, \eta)} e^{-i(a\xi + b\eta)} d\xi d\eta. \quad (4.5)$$

By setting  $a = kx/f$  and  $b = ky/f$  and taking the square complex modulus, one obtains the equation

$$|G(kx/f, ky/f)|^2 = \frac{k^2}{(2\pi f)^2} \left| \int_{-\infty}^{\infty} \int_{-\infty}^{\infty} f(\xi, \eta) e^{i\psi(\xi, \eta)} e^{-ik(x\xi + y\eta)/f} d\xi d\eta \right|^2. \quad (4.6)$$

By comparing this equation with the square complex modulus of the field at the focal plane (equation 4.3), one finds the relationship

$$|u(x, y, f)|^2 = |G(kx/f, ky/f)|^2. \quad (4.7)$$

From this last equality we have shown that the intensity of the field at the focal plane  $|u(z = f)|^2$ , is given by the Fourier transform of the combined phase imparted upon the incident field by both the phase element and the Fourier transform lens,  $|G|^2$ . So, if one wants a specific beam shape  $Q(x, y)$  at the focal plane, then by tuning the frequency components of the phase imparted upon the beam  $\phi(x, y)$  and the focal length  $f$  used then one can achieve the desired beam profile, such that

$$|G(kx/f, ky/f)|^2 = Q(x, y). \quad (4.8)$$

This problem is difficult in general, so the challenge in many beam shaping problems is to try and minimize the error between the actual beam profile and the desired profile, and, to further complicate the matter, many applications will require different notions of error to be used. For example, if one needs the energy distribution to be as close as possible to the desired profile, then the  $\ell_2$ -norm would be appropriate. However, if the maximum intensity is of concern, then the  $\ell_\infty$ -norm combined with the  $\ell_2$ -norm would be the appropriate notion of error.

It is possible to gain more insight into how difficult a beam shaping problem will be by reformulating the problem in terms of relevant length scales [2, 18]. The idea is to introduce a dimensionless parameter whose magnitude will reflect the validity of underlying assumptions, and so for a given value of this parameter one can intuitively understand the performance (or lack thereof) of the beam shaping system. This is done by reformulating the above situation in terms of the natural length scales of both the incoming field and the

desired field at the focal plane

$$I_{\text{input}} = |f(x, y)|^2 = |\hat{f}(x/\sigma, y/\sigma)|^2 \quad (4.9)$$

$$I_{\text{desired}} = Q(x, y) = \hat{Q}(x/d, y/d) \quad (4.10)$$

where  $\sigma$  is the characteristic length scale of the input field (typically the beam radius) and  $d$  is the characteristic length scale of the desired field. By expressing the fields in this way, we can now introduce the dimensionless parameter

$$\beta = \frac{2\pi\sigma D}{\lambda f}. \quad (4.11)$$

Using this dimensionless parameter, one can rewrite equations 4.5 and 4.8 as

$$G(\chi, \nu) = \int_{-\infty}^{\infty} \int_{-\infty}^{\infty} g(\xi, \eta) e^{-i(\chi\xi + \nu\eta)} e^{i\beta\hat{\phi}(\xi, \eta)} d\xi d\eta \quad (4.12)$$

$$|G(\chi, \nu)|^2 = \frac{4\pi^2 A}{\beta^2} Q(\chi/\beta, \nu/\beta) \quad (4.13)$$

where  $\chi = x\sigma k/f$ ,  $\nu = y\sigma k/f$ ,  $A$  is a constant, and  $\hat{\phi} = \beta\phi$ . From equation 4.12, it is clear that the functions  $g$  and  $G$  are related by a Fourier transform, so they must obey the uncertainty relation given by

$$\mu_g \mu_G \geq 1 \quad (4.14)$$

where  $\mu$  is the second moment. Now, if one were to choose the phase profile of the phase element  $\phi(x, y)$  such that equation 4.13 is satisfied, then one finds that  $\mu_G = \beta^2 \mu_Q$ . This then leads to the inequality

$$\beta^2 \mu_g \mu_Q \geq 1. \quad (4.15)$$

It can be seen that for large values of  $\beta$  this inequality can be readily satisfied. However, for very small values of  $\beta$  this inequality cannot be met and it will not be possible to produce the desired beam profile. From this, it can be seen that having a large value of  $\beta$  makes the beam shaping problem more tractable. The physical interpretation of  $\beta$  is that it is a measure of validity of geometric optics. It can be shown that when  $\beta$  is large a stationary phase method can be used to expand equation 4.12, and the lowest order term can be derived using a geometric optics approximation [2, 18].

In this section, the general problem of laser beam shaping has been introduced and formulated as a problem in Fourier analysis, and by rewriting everything in terms of natural length scales we can infer which types of beam shaping problems will be more tractable using geometrical optics approximations. The discussion so far has been kept very abstract, but in the next section the problem of interest will be introduced and these ideas will become more concrete.

### 4.2.2 Beam splitting phase grating

Now that the general theory behind laser beam shaping has been introduced, we move on to the specific problem at hand. The idea is to produce two nearly identical XUV beams through high-harmonic generation (HHG) using two nearly identical IR beams. The challenge is how to produce two nearly identical IR beams while minimizing the energy lost in the process. An additional requirement is that we can control the relative phase between these two IR beams. All of these requirements can be met through the use of a particular beam splitting phase grating [19–22].

As shown in section 4.2.1, the beam shape at the focal plane of a lens can be controlled through appropriate choice of a phase element and the spatially dependent phase  $\phi(x, y)$  which is imparted upon the incoming beam. We will still consider the schematic shown in figure 4.1. However, the phase element which will be considered in this section (the beam splitting phase grating) will only modify the phase in one dimension,  $\phi(x, y) = \phi(x)$ , and it will be a periodic function with a period of  $d$ ,  $\phi(x) = \phi(x + d)$ . If we expand the function  $P(x) = e^{i\phi(x)}$  in a Fourier expansion

$$P(x) = \sum_{n=-\infty}^{\infty} a_n e^{\frac{i2\pi n x}{d}} \quad (4.16)$$

$$a_n = \frac{1}{d} \int_{-d/2}^{d/2} P(\tilde{x}) e^{-\frac{i2\pi n \tilde{x}}{d}} d\tilde{x}, \quad (4.17)$$

then it can be shown (see Appendix SWPG) that each of the Fourier coefficients represents a diffracted beam and the energy contained in each diffracted beam is given by the square complex modulus of the Fourier coefficient  $|a_n|^2$  [20]. Thus, by making our phase element in figure 4.1 a phase grating, we have split the beam into many diffraction orders. We have defined the period of the phase grating by requiring  $\phi(x) = \phi(x + d)$ , however we have not yet determined its shape. This can be accomplished by specifying the distribution of energy into the various diffraction orders. Since we want to split the incoming beam into two duplicate beams, we are searching for  $d$ -periodic function that puts equal energy into two diffraction orders and a maximal amount of the input energy is put into those two orders. It can be shown (see Appendix SWPG) that the  $d$ -periodic function which meets these criteria is a  $0 - \pi$  square-wave phase grating given by

$$P(x, x_0) = \text{sign} \left( \cos \left( \frac{2\pi(x - x_0)}{d} \right) \right) \quad (4.18)$$

where  $x_0$  is an offset of position of the SWPG in the plane transverse to the optical axis [19, 22]. From this equation, it can be seen that the phase of the incoming beam is modulated by either  $0$  or  $\pi$  by the phase grating, and this is shown in figure 4.2 for the offset positions

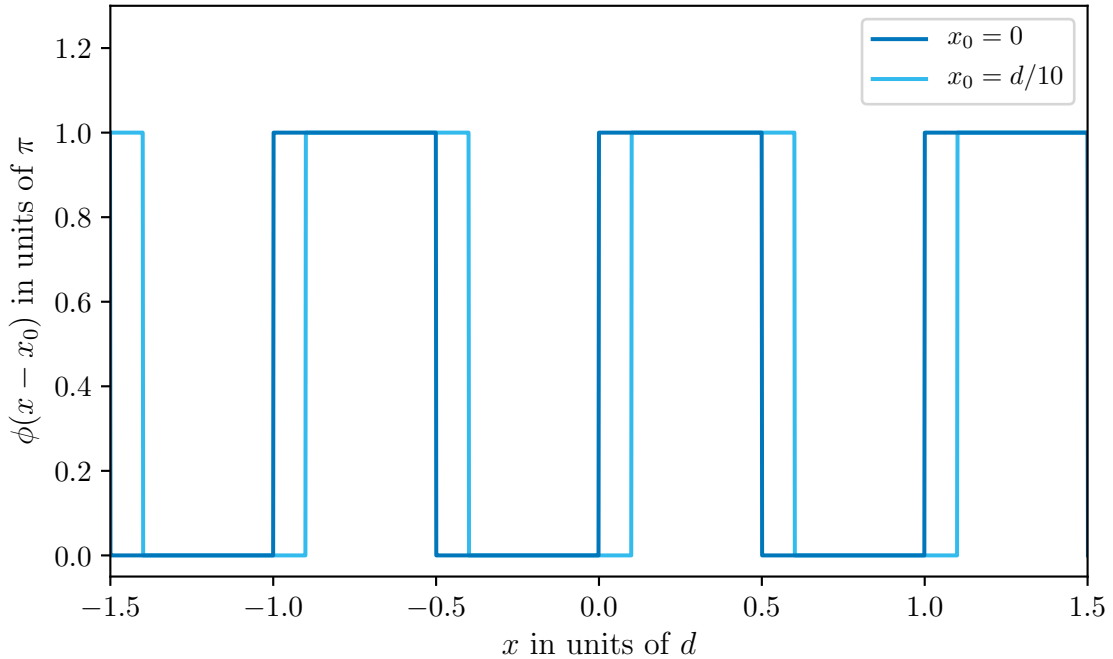


Figure 4.2: Plot of the phase function  $\phi(x - x_0)$  in units of  $\pi$  for a  $0 - \pi$  SWPG with a period of  $d$ . The dark blue (light blue) curve shows the phase function for  $x_0 = 0$  ( $x_0 = d/10$ ).

$x_0 = 0$  and  $x_0 = d/10$ .

From equation 4.16, we can calculate the Fourier coefficients  $a_n(x_0)$  for the SWPG for  $n = 0$  and  $n \neq 0$ . These Fourier coefficients determine how the energy is distributed between the different diffraction orders. For the zeroth-order case ( $n = 0$ ), we find that

$$\begin{aligned} a_0(x_0) &= \frac{1}{d} \int_{-d/2}^{d/2} \text{sign} \left( \cos \left( \frac{2\pi(\tilde{x} - x_0)}{d} \right) \right) d\tilde{x} \\ a_0(x_0) &= \frac{1}{d} \left[ - \int_{-\frac{d}{2}}^{-\frac{d}{4} + x_0} d\tilde{x} + \int_{-\frac{d}{4} + x_0}^{\frac{d}{4} + x_0} d\tilde{x} - \int_{\frac{d}{4} + x_0}^{\frac{d}{2}} d\tilde{x} \right] \\ a_0(x_0) &= 0. \end{aligned} \quad (4.19)$$

This demonstrates that zero energy is put into the zeroth-order diffraction for the  $0 - \pi$

SWPG. For the other diffraction orders, we find that

$$\begin{aligned}
a_n(x_0) &= \frac{1}{d} \int_{-d/2}^{d/2} \text{sign} \left( \cos \left( \frac{2\pi(\tilde{x} - x_0)}{d} \right) \right) e^{-\frac{i2\pi n \tilde{x}}{d}} d\tilde{x} \\
&= \frac{1}{d} \left[ - \int_{-\frac{d}{2}}^{-\frac{d}{4} + x_0} e^{-\frac{i2\pi n x}{d}} d\tilde{x} + \int_{-\frac{d}{4} + x_0}^{\frac{d}{4} + x_0} e^{-\frac{i2\pi n x}{d}} d\tilde{x} - \int_{\frac{d}{4} + x_0}^{\frac{d}{2}} e^{-\frac{i2\pi n x}{d}} d\tilde{x} \right] \\
&= \frac{1}{i2\pi n} \left[ e^{\frac{i\pi n}{2} - \frac{i2\pi n x_0}{d}} - e^{in\pi} + e^{\frac{i\pi n}{2} - \frac{i2\pi n x_0}{d}} - e^{-\frac{i\pi n}{2} - \frac{i2\pi n x_0}{d}} + e^{-in\pi} - e^{-\frac{i\pi n}{2} - \frac{i2\pi n x_0}{d}} \right] \\
&= \frac{1}{i\pi n} \left[ e^{\frac{i\pi n}{2} - \frac{i2\pi n x_0}{d}} - e^{-\frac{i\pi n}{2} - \frac{i2\pi n x_0}{d}} \right] = \frac{\sin(n\pi/2)}{n\pi/2} e^{-i\frac{2\pi n x_0}{d}} \\
a_n(x_0) &= \text{sinc}\left(\frac{n\pi}{2}\right) e^{-in\frac{2\pi x_0}{d}}.
\end{aligned} \tag{4.20}$$

Since  $\text{sinc}(n\pi/2) = 0$  for even integers  $n$ , we see that only the odd orders of diffraction from the SWPG are populated. The distribution of energy between the different diffraction orders is plotted in figure 4.3, and from this figure it is immediately clear that our choice of the  $0 - \pi$  SWPG has succeeded in putting most of the input energy equally into two diffraction orders, namely the  $\pm 1$  orders. The efficiency of this phase grating can be defined as

$$\eta = |a_1|^2 + |a_{-1}|^2 = \frac{8}{\pi^2} \approx 0.8106, \tag{4.21}$$

which means that approximately 81% of the input energy will be put into the two orders that we want. It should be noted that  $\sum_n |a_n|^2 = 1$ , which means that while we can't get perfect conversion of energy into only two orders this is still a lossless design.

With these Fourier coefficients in hand, we can now calculate the field profile at the focus. This is done by using equation 4.3,

$$\begin{aligned}
\tilde{S}(\tilde{x}) &= \frac{ikA}{2\pi f} e^{ikf} e^{i\frac{k\tilde{x}^2}{2f}} \int_{-\infty}^{\infty} S(x, x_0) e^{-ikx\tilde{x}/f} dx \\
\tilde{S}(\tilde{x}) &= \frac{ikA}{2\pi f} e^{ikf} e^{i\frac{k\tilde{x}^2}{2f}} \int_{-\infty}^{\infty} E(x) \sum_{n=-\infty}^{\infty} a_n(x_0) e^{-i\frac{2\pi n x}{d}} e^{-ikx\tilde{x}/f} dx \\
\tilde{S}(\tilde{x}) &= \frac{ikA}{2\pi f} e^{ikf} e^{i\frac{k\tilde{x}^2}{2f}} \sum_{n=-\infty}^{\infty} a_n(x_0) \int_{-\infty}^{\infty} E(x) e^{-i\frac{2\pi n x}{\lambda f} (\tilde{x} - n\frac{\lambda f}{d})} dx \\
\tilde{S}(\tilde{x}) &= \sum_{n=-\infty}^{\infty} a_n(x_0) \tilde{E}(\tilde{x} - n\frac{\lambda f}{d})
\end{aligned} \tag{4.22}$$

where

$$\tilde{E}(\tilde{x}) = \frac{ikA}{2\pi f} e^{ikf} e^{i\frac{k\tilde{x}^2}{2f}} \int_{-\infty}^{\infty} E(x) e^{-ikx\tilde{x}/f} dx, \tag{4.23}$$

$x_n = n\lambda f/d$ ,  $S(x, x_0) = E(x)P(x, x_0)$  is the field after the phase grating, and  $A$  is a constant

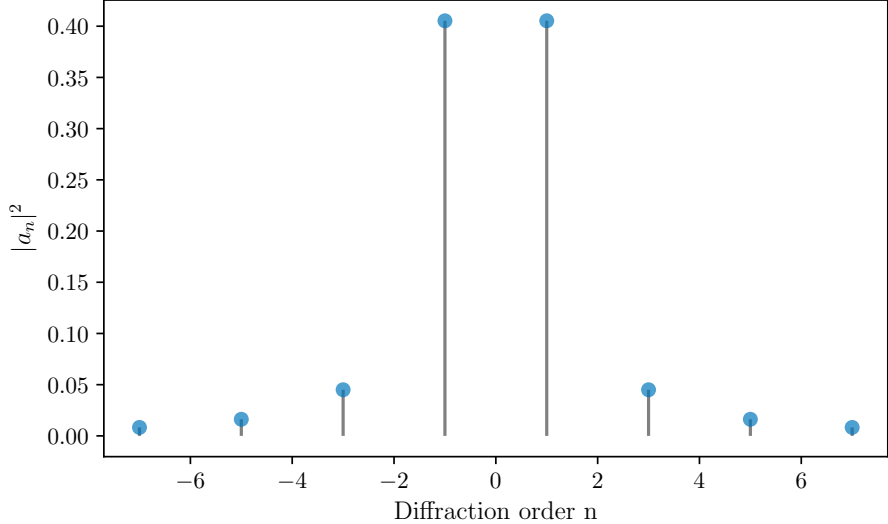


Figure 4.3: Square complex modulus of the Fourier coefficients  $a_n$  of the  $0 - \pi$  SWPG. The square complex modulus is proportional to the energy put into each diffraction order. As can be seen from figure, the  $\pm 1$  orders have the most energy put into them at  $4/\pi^2 \approx 41.1\%$  each. All even orders have zero energy.

to account for the  $y$  dimension in equation 4.3 which has been neglected for clarity in this discussion. Substituting in equation 4.20 into equation 4.22 yields

$$\tilde{S}(\tilde{x}, x_0) = \sum_{n \neq 0} \text{sinc}\left(\frac{n\pi}{2}\right) \tilde{E}(\tilde{x} - \tilde{x}_n) e^{-in\frac{2\pi x_0}{d}} \quad (4.24)$$

which is the field at the focal plane. From this equation, the role of the transverse offset  $x_0$  immediately becomes clear. It is used to control the relative phase between diffraction orders of the SWPG. The phase difference between the two most populated orders, the  $n = \pm 1$  orders, is given by

$$\Delta\phi_{\pm 1} = 2\left(\frac{2\pi x_0}{d}\right). \quad (4.25)$$

Therefore, by controlling the offset of the SWPG we can control the relative phase between the two orders of interest over a range of  $[0, 4\pi]$ , two full periods of the fundamental wavelength. Additionally, one can begin to see from equation 4.3 that the intensity profile at the focal plane consists of copies of the focused input field at  $x_n = n\lambda f/d$ . An example intensity profile at the focal plane is shown in figure 4.4. In this figure the  $\pm 1$  orders are shown to be the most intense, and the phase is extracted for two different grating offset positions  $x_0$ . This calculated by numerically propagating the beam profile and SWPG in figure 4.5.

So far, we have demonstrated that a binary  $0 - \pi$  SWPG can theoretically achieve our

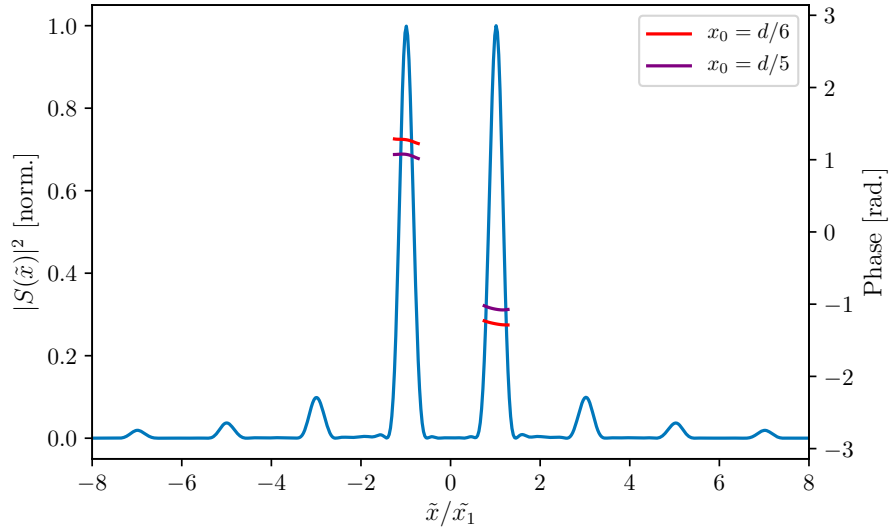


Figure 4.4: Intensity profile  $S(\tilde{x})$  at the focal plane. Horizontal units are scaled by the spacing between orders,  $\tilde{x}_1 = \lambda f/d$ . Phase is also plotted for two different offset positions  $x_0 = d/3$  and  $x_0 = d/5$ . This demonstrates the ability of the SWPG to generate two sources and control the relative phase between them. Calculated by numerically propagating the beam profile and SWPG in figure 4.5.

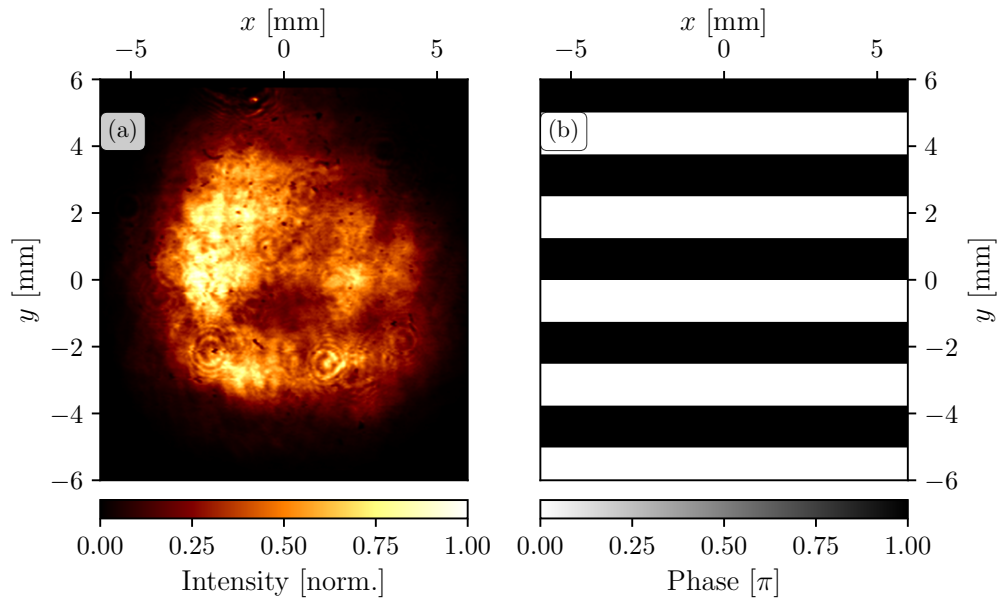


Figure 4.5: (a) Intensity profile of the input beam measured by a thermal camera. (b) Phase imparted by  $0 - \pi$  SWPG with a grating period of  $d = 2.5$  mm.

requirements of an efficient beam duplicator with phase control between the two duplicate beams. However, all of the results shown above have been only considering the monochromatic case, and for the experiments of interest we will use a femtosecond IR pulse with bandwidth on the order of 50 nm. This presents a challenge because the SWPG will be constructed by etching a fused-silica plate to have the desired phase step of  $\pi$ , and the inherent dispersion as the beam passes through the material means that the step will be  $\pi$  for only one wavelength. Thus, it is important to get a handle on how an imperfect non- $\pi$  phase step affects the properties of the SWPG. To do this, we introduce a non- $\pi$  phase step into the above analysis by a parameter  $\zeta$ , such that the  $0 - \pi$  step becomes a  $0 - \zeta\pi$  step,

$$\phi(x, x_0, \zeta) = \zeta\phi(x, x_0). \quad (4.26)$$

Going back to 4.19, we can calculate the zero-order term for  $\zeta \neq 1$ ,

$$\begin{aligned} a_0(x_0, \zeta) &= \frac{1}{d} \int_{-\frac{d}{2}}^{\frac{d}{2}} e^{\zeta\phi(\tilde{x}, x_0)} d\tilde{x} \\ &= \frac{1}{d} \left[ \int_{-\frac{d}{2}}^{-\frac{d}{4}+x_0} e^{i\zeta\pi} d\tilde{x} + \int_{-\frac{d}{4}+x_0}^{\frac{d}{4}+x_0} d\tilde{x} + \int_{\frac{d}{4}+x_0}^{\frac{d}{2}} e^{i\zeta\pi} d\tilde{x} \right] \\ &= \frac{1}{d} \left[ \frac{d}{2} + \frac{d}{2} e^{i\zeta\pi} \right] = \frac{e^{i\zeta\pi/2}}{2} \left[ e^{i\zeta\pi/2} + e^{-i\zeta\pi/2} \right] \\ a_0 &= \cos\left(\frac{\pi}{2}\zeta\right) e^{i\zeta\pi/2}. \end{aligned} \quad (4.27)$$

Previously, for  $\zeta = 1$  we found that the zeroth-order term was not populated by the SWPG ( $a_0 = 0$ ), however from the above equation we can clearly see that the non- $\pi$  phase step has introduced a population in the zeroth-order. The percent of the total input energy that is placed into the zeroth order is  $|a_0(\zeta)|^2 = \cos^2(\zeta\pi/2)$ . Furthermore, from equation 4.20 we can also calculate the other orders for  $\zeta \neq 1$ ,

$$\begin{aligned} a_n(x_0, \zeta) &= \frac{1}{d} \int_{-\frac{d}{2}}^{\frac{d}{2}} e^{\zeta\phi(\tilde{x}, x_0)} e^{-in\frac{2\pi\tilde{x}}{d}} d\tilde{x} \\ &= \frac{1}{d} \left[ \int_{-\frac{d}{2}}^{-\frac{d}{4}+x_0} e^{i\zeta\pi-in\frac{2\pi\tilde{x}}{d}} d\tilde{x} + \int_{-\frac{d}{4}+x_0}^{\frac{d}{4}+x_0} e^{-in\frac{2\pi\tilde{x}}{d}} d\tilde{x} + \int_{\frac{d}{4}+x_0}^{\frac{d}{2}} e^{i\zeta\pi-in\frac{2\pi\tilde{x}}{d}} d\tilde{x} \right] \\ a_n(x_0, \zeta) &= \text{sinc}\left(\frac{n\pi}{2}\right) \sin\left(\frac{\pi}{2}\zeta\right) e^{i\frac{\pi}{2}(\zeta-1)} e^{-in\frac{2\pi x_0}{d}} \\ a_n(x_0, \zeta) &= a_n(x_0) \sin\left(\frac{\pi}{2}\zeta\right) e^{i\frac{\pi}{2}(\zeta-1)}. \end{aligned} \quad (4.28)$$

From this equation, we can see that the non- $\pi$  phase step has not populated the even diffraction orders, but the odd orders have an overall phase shift and are reduced in amplitude by a factor of  $\sin(\zeta\pi/2)$ . This should be expected because we saw from equation 4.27 that the

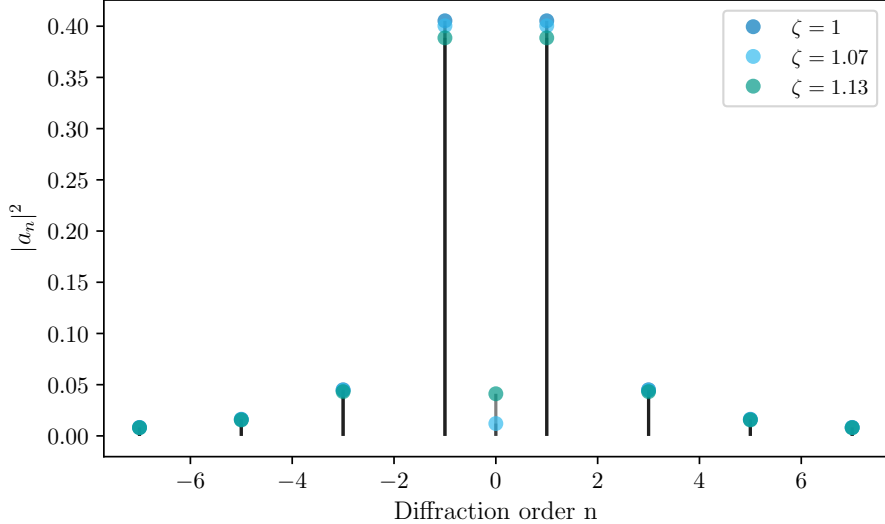


Figure 4.6: Square complex modulus of the Fourier coefficients  $a_n$  of the  $0 - \zeta\pi$  SWPG for several values of  $\zeta$ . The square complex modulus is proportional to the energy put into each diffraction order. As can be seen from figure, the  $\pm 1$  orders have the most energy put into them even for  $\zeta \neq 1$ . All non-zero even orders have zero energy.

zeroth-order was populated by a fractional energy of  $|\cos(\zeta\pi/2)|^2$ . Since this is a lossless system ( $\sum_n |a_n|^2 = 1$ ), the energy that is populating the zeroth-order is coming from all of the odd orders that were populated. This redistribution of energy by  $\zeta \neq 1$  is shown in 4.6.

From equations 4.27 and 4.28, we now have a notion of how the SWPG is behaving across the bandwidth of our femtosecond pulses. In particular, so long as  $\zeta$  is close to 1, then the  $\pm 1$  orders are still the most intense, and as the grating offset  $x_0$  is varied the phase difference between the  $\pm 1$  orders remains  $\Delta\phi_{\pm 1} = 2\left(\frac{2\pi x_0}{d}\right)$  even though the overall spectral phase is modified by a factor of  $e^{i\zeta\pi/2}$ . To set a scale for what  $\zeta$  close to 1 means, consider the case when the zeroth-order is equal in amplitude to the the  $\pm 3$  orders,  $|a_0(x_0, \zeta)| = |a_{\pm 3}(x_0, \zeta)|$ . In this case,  $|\xi - 1| = |\frac{2}{\pi} \tan^{-1}(3\pi/2) - 1| \approx 0.13$ . Therefore, it is reasonable to state the  $0 - \pi$  SWPG maintains its phase control duplication properties for  $|\zeta - 1| < 0.13$ .

#### 4.2.3 Square-wave phase grating design for high-harmonic generation

With the theory behind the SWPG well established, the specific grating parameters that were chosen with HHG in mind will be discussed in this section. The laser source that will be considered is the output of a HE-TOPAS optical parametric amplifier produced by Light Conversion. The TOPAS is pumped by a Spitfire ACE Ti:Sapphire system from Spectra-Physics. The Spitfire ACE system is capable of producing 12 mJ, 60 fs (20 nm

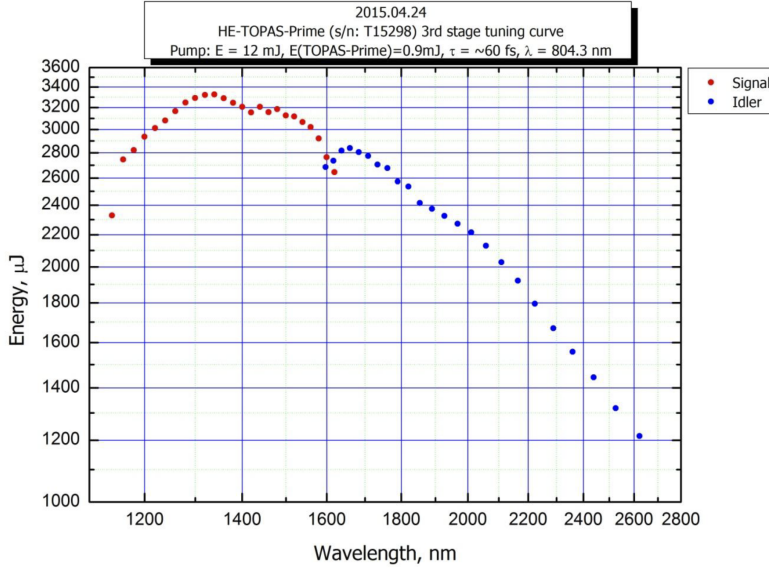


Figure 4.7: Pulse energy output of the TOPAS used in the experiments described within this chapter. The optimal output energy of the TOPAS can be seen to be around 1350 nm. This is the wavelength that was selected as the design wavelength for the SWPG.

FWHM bandwidth) pulses at 1 kHz. Using this system, the TOPAS is able to generate up to a combined 6 mJ of signal and idler. The signal wavelength range is from 1200 nm to 1600 nm, and within this range the TOPAS can output a nominally 70 fs pulse of up to 3 mJ with a tuneable central wavelength. A design wavelength of 1350 nm was chosen for the SWPG because the TOPAS performance is optimal around this wavelength (see figure 4.7).

Once the design wavelength for the phase grating is selected, then the physical size,  $L$ , of the step is determined by dispersion of the material selected from the relationship  $\phi = \pi = 2\pi nL/\lambda$ . For our phase gratings, Corning HPFS 7980 was used, and with this material  $L \approx 0.47\mu m$ . The refractive index and the corresponding  $\zeta$  parameter is shown in figure 4.8. The limitation that  $\zeta = 1$  for only the design wavelength can be relaxed somewhat by introducing a nonzero angle of incidence between the incoming beam and the SWPG to effectively increase the optical path length of the step. If this angle is  $\theta$ , then the  $\zeta$  parameter can be written as

$$\zeta(\lambda, \theta) = \sec \theta \left( \frac{n(\lambda)\lambda_0}{\lambda n_0} \right) \quad (4.29)$$

where  $\lambda_0$  is the design wavelength and  $n_0$  is the refractive index at the design wavelength. This factor is shown in figure 4.8. From this figure, it is clear that even though the SWPG is designed for a specific wavelength it can be used over a broad range of wavelengths that

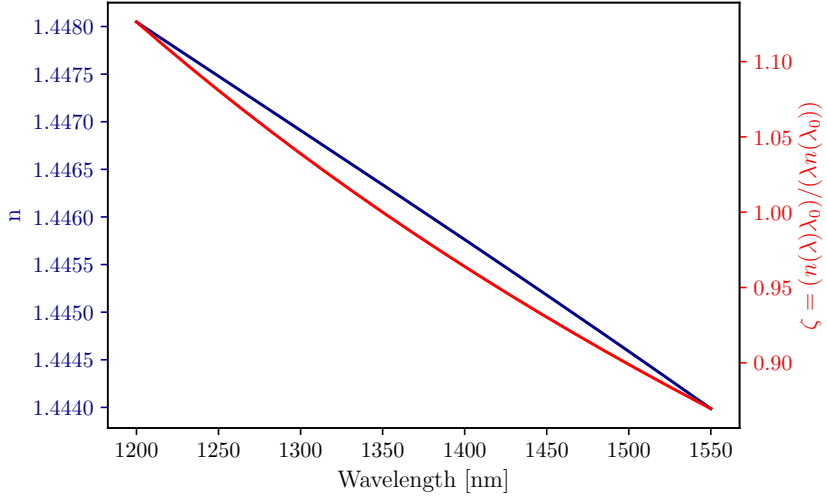


Figure 4.8: Refractive index (blue curve and axis) and the  $\zeta$  parameter (red curve and axis). For a 70 nm bandwidth pulse centered at 1350 nm,  $\zeta - 1$  varies from -0.026 to 0.027 assuming normal incidence.

are longer than the design wavelength. Of course, at higher angles of incidence propagation effects might become non-negligible, and those effects are neglected here.

The final remaining design parameter that must be considered is the choice of grating period. The choice of period is critical for the performance of the SWPG, and must be chosen with care. To get insight into how to select the correct period, we will reintroduce the  $\beta$  parameter from equation 4.11. For the specific situation we are considering, the  $\beta$  parameter is

$$\begin{aligned}\beta &= \frac{2\pi\sigma D}{\lambda f} = \frac{2\pi\sigma(\frac{\lambda f}{d})}{\lambda f} \\ &= 2\pi\left(\frac{\sigma}{d}\right)\end{aligned}\tag{4.30}$$

where  $\sigma$  is the input beam radius and  $D = \tilde{x}_1 = \lambda f/d$  is that characteristic length scale at the focal plane because it represents the separation between the different diffraction orders in the focal plane. The beam profile at the focus can be calculated for various parameters of  $\beta$ , and is shown in figure 4.10. In the limit as  $\beta \rightarrow 0$ , the condition  $d \gg \sigma$  must hold, and this condition implies that the source separation is approaching the waist radius of each diffraction order  $\tilde{\sigma}$ . Once the separation between orders becomes comparable to the waist ( $\tilde{\sigma} \approx \tilde{x}_1$ ), then each diffraction order will strongly interfere with its neighboring orders. The effect of this interference is that our sources can no longer be thought of as independent beams, and as the grating offset  $x_0$  is varied there will be a strong modulation of both the amplitude and phase of each of diffraction order. This can be seen by using equation 4.22

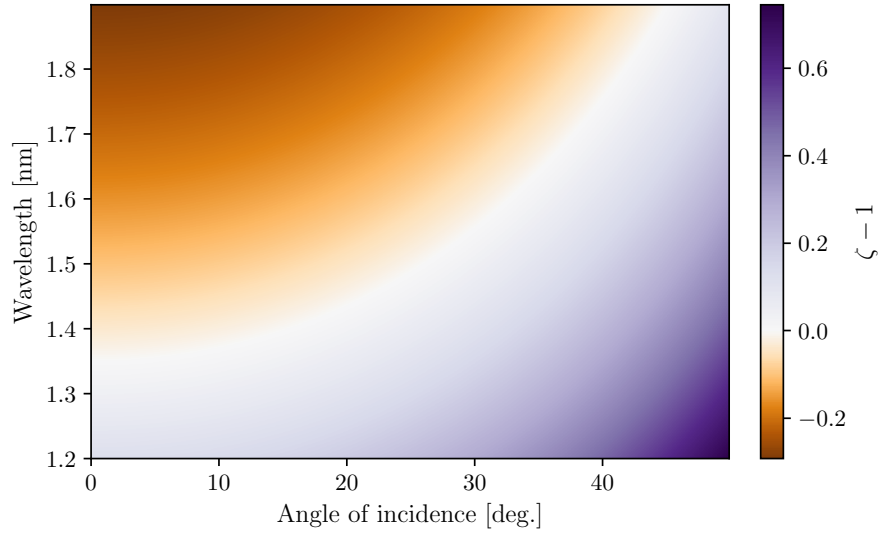


Figure 4.9: Non- $\pi$  phase step parameter  $\zeta(\lambda, \theta)$  calculated for a range of relevant wavelengths and incident angles. The ability to effectively tune the optical path length of the step enables the SWPG to be used for a much larger range of wavelengths than are longer than the initial design wavelength.

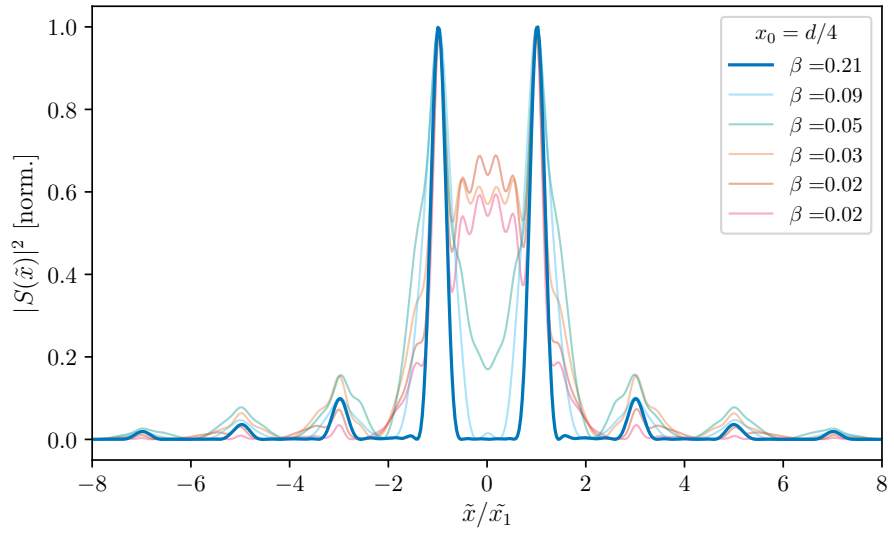


Figure 4.10: Calculation of intensity at the focal plane of the SWPG for various parameters of  $\beta$ . Calculation is done by numerically propagating the measured beam profile shown in 4.5.  $\beta$  is varied by adjusting the radius of the input beam profile. As  $\beta \rightarrow 0$ , one can see that the performance of the SWPG deteriorates and no longer produces well separated sources.

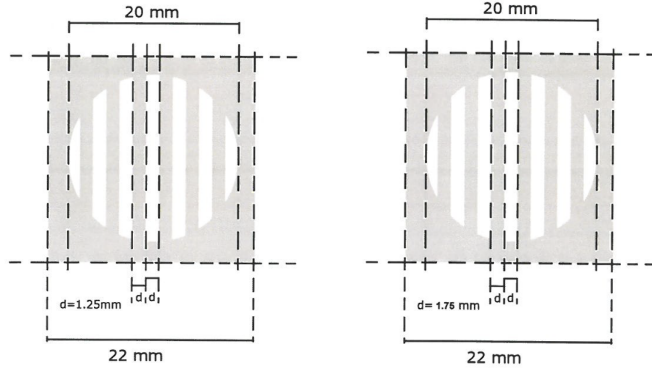


Figure 4.11: Schematic of the two SWPG which were purchased from Silios. They are constructed by etching the phase step in Corning HPFS 7980 fused-silica.

to write the intensity at the focal plane

$$\begin{aligned}
 |\tilde{S}(\tilde{x}, \phi_1)|^2 &= \sum_{n=-\infty}^{\infty} \sum_{n'=-\infty}^{\infty} a_n \tilde{E}(\tilde{x} - \tilde{x}_n) e^{-in\phi_1} a_{n'} \tilde{E}(\tilde{x} - \tilde{x}_{n'}) e^{-in'\phi_1} \\
 &= \sum_{q=-\infty}^{\infty} e^{-iq\phi_1} \sum_{n=-\infty}^{\infty} a_n \tilde{E}(\tilde{x} - \tilde{x}_n) a_{n-q} \tilde{E}(\tilde{x} - \tilde{x}_{n-q}) \\
 &= \sum_{n=-\infty}^{\infty} \tilde{E}_{2n+1}^2(\tilde{x}) + 2 \sum_{q=1}^{\infty} \cos(2q\phi_1) \sum_{n=-\infty}^{\infty} \tilde{E}_{2n+1}(\tilde{x}) \tilde{E}_{2n-2q+1}(\tilde{x})
 \end{aligned} \tag{4.31}$$

where  $\tilde{E}_n(\tilde{x}) = |a_n| \tilde{E}(\tilde{x} - \tilde{x}_n)$ . The second term demonstrates that as the grating offset  $x_0$  is varied, the intensity of a diffraction order  $2n + 1$  will be modulated by an oscillatory term  $\cos(2q\phi_1)$ . The amplitude of this oscillation is determined by the overlap of the diffraction orders. Thus, for a grating such that  $d \gg \sigma$  the oscillations will be very large because the source separation will be comparable to the beam waist of each order.

While it has become clear that choosing a grating period such that  $\sigma \gg d$  is the ideal case for the performance of the SWPG as a beam duplicator, there is another consideration that must be made for our specific application. In particular, we would like to generate high-harmonics from the  $\pm 1$  orders, and in order to do that we must send both sources through a gas medium generated by a gas jet in vacuum. This becomes increasingly difficult to handle as the source separation becomes large because the nozzle diameter must also increase, and the throughput of the nozzle increases quadratically with the diameter [23]. Since this needs to be done in vacuum, at a certain point the pumping requirements become untenable. So, in light of these considerations, the grating periods that were chosen were 2.5 mm and 3.5 mm. A schematic of the gratings are shown in figure 4.11. Using these gratings and a  $f = 400$  mm lens at 1450 nm, we are able to achieve a source separation of 331  $\mu m$  and 464

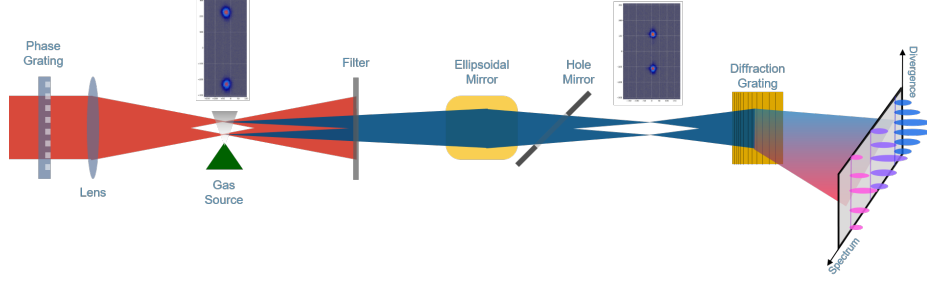


Figure 4.12: Schematic of the two-source HHG experiment performed in the TABLE. A  $0 - \pi$  SWPG is used to generate two intense lobes at the focus of a lens. These lobes will generate XUV beams which will interfere in the far-field. An ellipsoidal mirror is used to refocus the XUV beams before going onto the spectrometer.

$\mu\text{m}$  for the grating periods  $d = 3.5 \text{ mm}$  and  $d = 2.5 \text{ mm}$ . These parameters correspond to  $\beta \approx 7$  for the  $3.5 \text{ mm}$  grating and  $\beta \approx 10$  for the  $2.5 \text{ mm}$  grating for an input beam radius of  $\sigma = 4 \text{ mm}$ .

### 4.3 Two-source high-harmonic generation

To demonstrate that the  $0 - \pi$  SWPG can be used as a femtosecond beam duplicator with relative phase control, we will generate harmonics from the  $\pm 1$  diffraction orders. This experiment will be performed in the transient-absorption beamline (TABLE), and a schematic is shown in figure 4.12. A  $0 - \pi$  SWPG will be used to generate two intense lobes at the focal plane of a  $\text{CaF}_2$  plano-convex lens with a focal length of 400 mm. A piezoelectric pulsed valve gas jet with a nozzle diameter of  $500 \mu\text{m}$  is placed near the focus to deliver a gas medium in which high-harmonics are generated. The gas that will be used for generation will be argon. An image of the two sources is shown in 4.13. The laser which was used for this experiment is the output of an HE-TOPAS pumped by the Spitfire laser system. We will be working with a central wavelength of 1435 nm and a pulse energy of 2 mJ. The harmonics that are generated will pass through a 200 nm Al filter to filter out the fundamental. In the energy ranges that we will be generating harmonics, Al will transmit harmonics in the energy range of 20 - 72 eV. After the metallic filter, the XUV will be passed through a mirror with a hole in it and it will be refocused by an ellipsoidal mirror with a demagnification of 3. The XUV will then enter the spectrometer which consists of a Hitachi 1200 lines/mm variable line spaced (VLS) grating with a microchannel plate (MCP)/phosphor detector. The output of the phosphor is imaged by an Andor Neo 5.5 camera. The VLS grating focuses spectrally onto a flat-field, but in the transverse dimension it maintains the spatial profile. With this spectrometer we are able to simultaneously get spatial and spectral information about the incoming light.

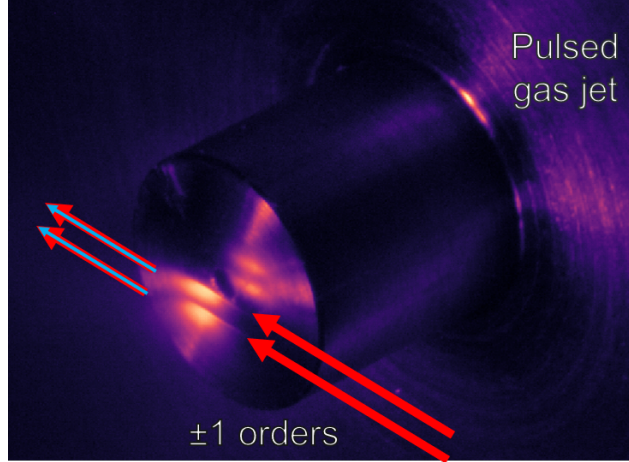


Figure 4.13: False color image of the two sources from the SWPG driving ionization in a gas medium delivered by the piezo gas jet shown in the image. Two sources follow the red arrows, and the XUV that is generated is shown by blue arrows.

The harmonics that are generated from this setup are shown in figure 4.14. Along the spatial dimension (labeled sensor position in the figure), one can immediately see a fringe pattern. These fringes are from the two sources that are generating harmonics. The intuitive way to understand the spatial frequency of these fringes is by thinking of them in terms of a Young's double slit. From this perspective, the wavelength dependence of the spatial frequencies present in the spatial profile of harmonic order  $q$  is

$$k_q = q \frac{2\pi\Delta x}{L\lambda} \propto q\hbar\omega \quad (4.32)$$

where  $L$  is the distance from the two sources to the detector and  $\Delta x$  is separation between the two sources. This linear dependence of the spatial frequency on photon energy is clear seen in figure 4.14.

The position of the fringe pattern in the spatial profile of the harmonics is determined by the relative phase between the two HHG sources. Therefore, any phase shift between the two sources will be imprinted upon the spatial profile of the harmonics as a fringe shift. We will utilize this sensitivity to demonstrate the capabilities of the SWPG. If we generate harmonics from the  $\pm 1$  orders of the SWPG, then as the grating offset  $x_0$  is varied we would expect the fringe pattern for harmonic order  $q$  to shift by a factor of  $q$  multiplied by the phase shift between the two IR sources. Thus, for a translation of the grating by  $\Delta x_0$  the  $q$ -th harmonic fringe pattern will shift by  $4q\pi\Delta x_0/d$ . If the grating is scanned through its full period of  $d$ , then the phase difference between the two harmonic beams of order  $q$  will span a range of phases up to  $4q\pi$ . Due to the high non-linearity of HHG, this technique is very sensitive to small shifts in phase between the two beams, and it is precisely

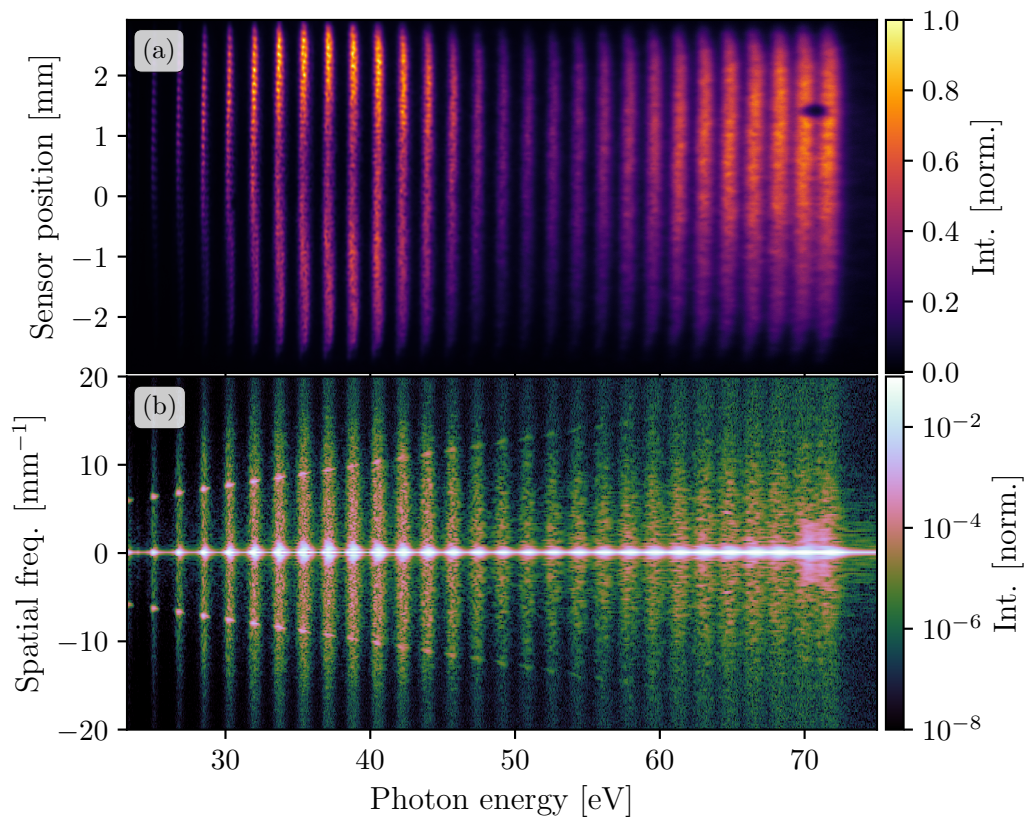


Figure 4.14: (a) Reference harmonic spectrum generated with a  $0 - \pi$  SWPG. The fringes along the sensor position dimension are due to interference between the two XUV sources that are generated. The position of the fringe pattern is determined by the relative phase between the two sources. This relative phase can be controlled by the SWPG. (b) Power spectrum of the Fourier transform of the above image along the sensor position dimension. Clear peaks can be seen corresponding to the spatial frequency for each harmonic order. The linear dependence of the spatial frequency on photon energy is also seen.

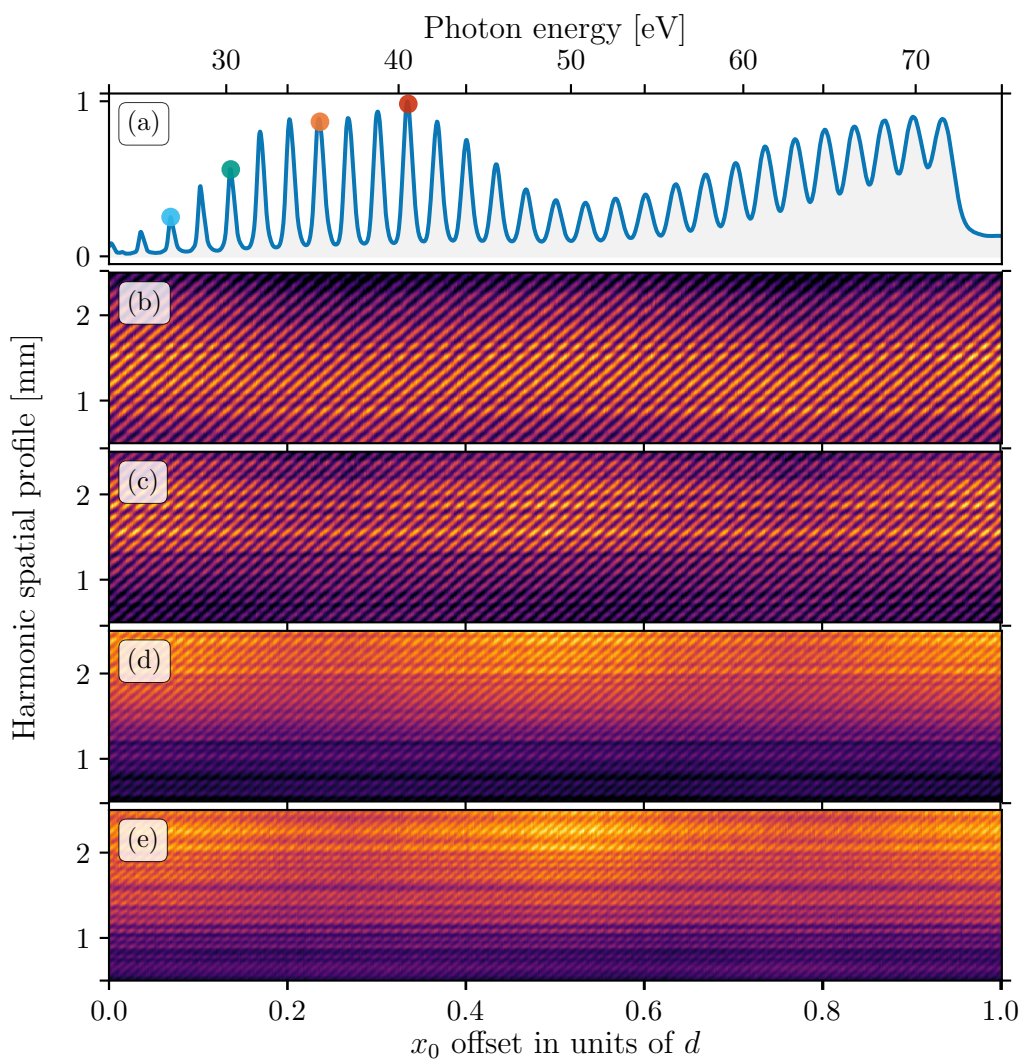


Figure 4.15: (a) Reference harmonic spectrum with dots showing the harmonic orders whose spatialgrams are plotted below. (b)-(e) Spatialgrams for harmonic orders 29, 33, 39, and 45. Tilted fringe pattern shows fringe shift due to phase shift induced by translating the phase grating. Modulations with a period od  $d/2$  arise because of interference between the two generating sources.

this sensitivity that will be leveraged in later experiments to extract more information in transient absorption experiments. It is important to be clear that we are not looking to measure the absolute phase difference between the two sources. Instead, we are primarily interested in our ability to measure a very small phase difference between the two sources introduced by the SWPG.

The measured effect of translating the grating is shown in figure 4.15. Four harmonics orders have been selected and their spatial profile have been plotted versus grating offset position  $x_0$ . These types of figures will be referred to as a spatialgram. Each spatialgram exhibits a tilted fringe pattern that corresponds to the fringe shift induced by a phase shift between the two XUV sources. As expected, the higher order harmonics have a higher frequency fringe pattern because of their shorter wavelength. If one counts the number of fringes over the full grating period scan, then one would find  $2q$  fringes for harmonic order  $q$ . This provides a direct measure of the harmonic order  $q$  and is used in a calibration scheme for the spectrometer (see chapter on calibration). The ability to measure the harmonic order  $q$  from the spatialgram verifies that the SWPG is able to control the phase difference between the two IR sources with a precision of a few mrad.

An additional feature of the spatialgrams in figure 4.15 is a slower modulation that has a period of  $d/2$ . This effect is present for all harmonic orders, and appears in a very similar way. This slower modulation is due to the interference between the two IR sources that were introduced in equation 4.31. The modulations with a period of  $d/2$  is due to interference between the  $\pm 1$  and  $\mp 1$  diffraction orders. There is also a modulation with a period of  $d$  that is present in the spatialgrams. This modulation is due to interference between the 0th order and the  $\pm 1$  orders. In general, the frequency of the modulations is related to the separation between the diffraction orders that are interfering. These modulations are a limiting factor in using the phase grating for Fourier transform spectroscopy in the XUV.

Another interesting result from these measurements is that the symmetry of the attosecond pulse train (APT) that is generated can be observed because we are, in effect, measuring the interferometric autocorrelation of the XUV that is generated [24–27]. This is done either by looking at the zeroth-order diffraction off the VLS grating, or by integrating spectrally and looking at the combined spatial profile versus the grating offset. The latter technique is used to generate figures 4.16 and 4.17. In figure 4.16, the pulses that make up the APT can be clearly seen. Since the phase grating is limited to a scan range of  $4\pi$  between the two IR sources, we would expect to see only four pulses (one per half-cycle), and this is exactly what is observed. This can also be done in the case where the harmonics are generated using a two-color field consisting of the fundamental wavelength and its second harmonic. In this instance, the symmetry of the field is broken, and one should expect to see an attosecond pulse once per cycle of the fundamental [28–30]. That exact case is shown in figure 4.17. In principle, by Fourier transforming these traces, one should be able

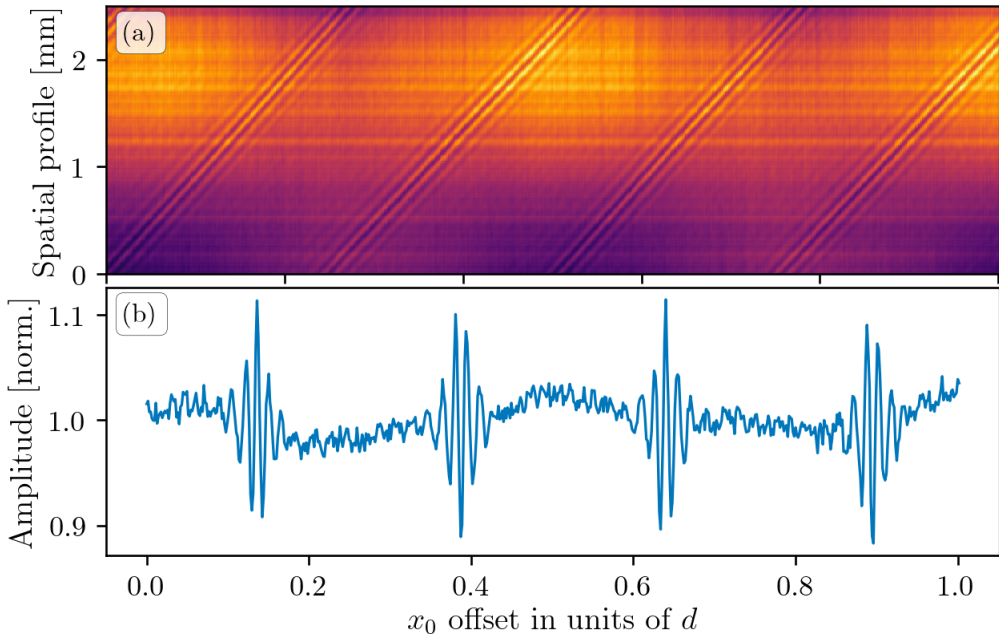


Figure 4.16: (a) Spatialgram of all harmonic orders combined. Diagonal stripes show the attosecond pulses that make up the APT. (b) Lineout from the full spatialgram.

to recover the harmonic spectrum with a spectral resolution of  $\omega/2$ .

#### 4.4 Conclusion

In this chapter, the general concept of laser beam shaping was introduced, and the methods therein were applied to the specific problem of generating duplicates of a femtosecond IR pulse with precise control over their relative phase. The diffractive optical element that was shown to meet these demands is a  $0 - \pi$  square-wave phase grating (SWPG). Its properties were discussed, and the final design parameters were chosen to optimize the SWPG for high-harmonic generation. The properties of the SWPG were demonstrated by generating high-harmonics and observing their corresponding fringe shifts. This experiment has also demonstrated the ability to measure small phase shifts between the two relative phase locked XUV beams. This property will be leveraged in experiments described in the following chapters.

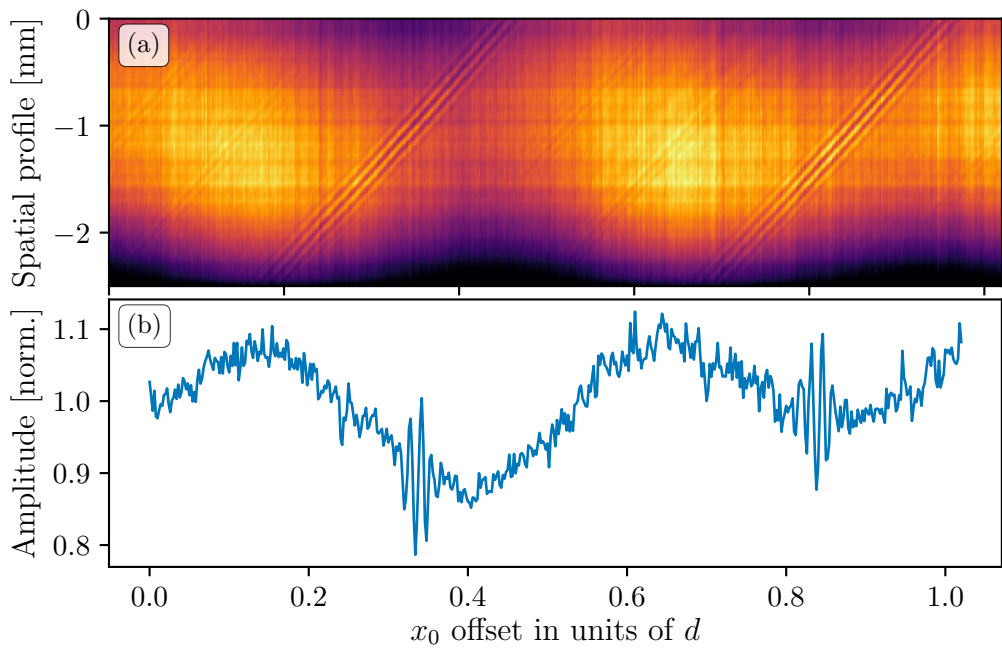


Figure 4.17: (a) Spatialgram of all harmonic orders combined. Diagonal stripes show the attosecond pulses that make up the APT. A second harmonic field was added to break the symmetry and generate even harmonics. (b) Lineout from the full spatialgram. Only two attosecond bursts are seen, which is expected from the asymmetric two-color generation field. The increased modulation with a period  $d/2$  is due to the stronger interference between the two sources.

# Chapter 5

## TWO-SOURCE REFRACTIVE INDEX MEASUREMENT

### 5.1 Introduction

In chapter 4, the  $0 - \pi$  square-wave phase grating (SWPG) was introduced as a means of generating two intense duplicates of an input femtosecond mid-IR pulse. An additional element of the SWPG is that it enables precise control over the relative phase between these two sources. When used to generate high harmonics, this scheme enables the generation of two XUV sources whose relative phase is well controlled by the SWPG, and any small phase shift between the two harmonic beams is imprinted upon their interference pattern as a fringe shift in the far-field. The idea is to now leverage this sensitivity to measure an induced phase shift between the two XUV sources. In the experiment described in this chapter, the phase shift will be induced by introducing a thin condensed matter sample into only one of the two XUV sources. Doing so enables us to extract both the real and imaginary part of the refractive index over a broad range of photon energies in the XUV.

### 5.2 Complex refractive index

The complex refractive index depends strongly on photon energy, and a cartoon of this is shown in figure 5.1. We are interested in the refractive index in the XUV energy region, and in this energy region there are many resonances that correspond to transitions of core-level electrons to unoccupied states near the Fermi level (for the case of a condensed matter system)[3, 31]. Complicated fine structure can emerge near these resonances that correspond to the local electronic and geometric environment[3, 31]. Thus, the ability to measure both the real and imaginary parts of the complex refractive index can be important for many experiments using XUV light generated by HHG[32, 33].

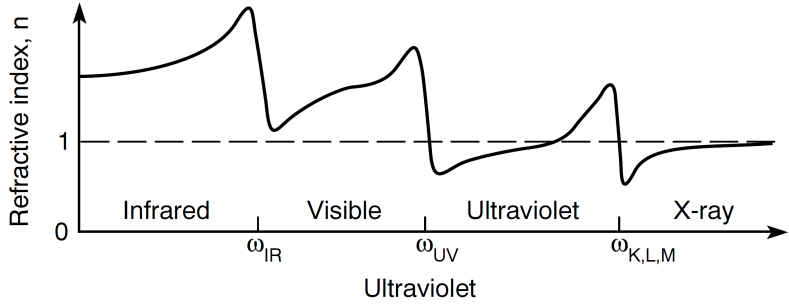


Figure 5.1: Schematic of the real part of the refractive index versus photon energy. Example resonances are shown in the IR, the visible/UV, and in the XUV/soft x-ray regimes. In general, the refractive index approaches 1 at higher photon energies. Adapted from [3].

In general, the complex refractive index can be written as[3]

$$n(\omega) = 1 - \left( \frac{n_a r_e \lambda^2}{2\pi} \right) \left[ f_1(\omega) - i f_2(\omega) \right] \quad (5.1)$$

where  $n_a$  is the number density,  $\omega$  ( $\lambda$ ) is the photon energy (wavelength), and

$$r_e = \frac{e^2}{4\pi\epsilon_0 mc^2} \quad (5.2)$$

is the classical electron radius. By introducing the parameters  $\beta$  and  $\delta$ , such that

$$\delta = \frac{n_a r_e \lambda^2}{2\pi} f_1(\omega) \beta = \frac{n_a r_e \lambda^2}{2\pi} f_2(\omega), \quad (5.3)$$

then the refractive index  $n$  can be written as

$$n(\omega) = 1 - \delta + i\beta. \quad (5.4)$$

The values of both  $\delta$  and  $\beta$  have been tabulated for elements from hydrogen up to uranium in the range of 10 eV to 30 keV[34], and their values are generally smaller than unity when far from resonance.

Now that we've established the form of the refractive index, we will consider the case of propagation through a dispersive medium [3]. The idea is to consider a plane wave of the form

$$\mathbf{E}(\mathbf{r}, t) = \mathbf{E}_0 e^{-i(\omega t - \mathbf{k} \cdot \mathbf{r})}, \quad (5.5)$$

and assume that the dispersion of the medium takes the form

$$\frac{\omega}{k} = \frac{c}{n} = \frac{c}{1 - \delta + i\beta}. \quad (5.6)$$

With these relationships, one can write the field in the propagation direction defined by  $\mathbf{k} \cdot \mathbf{r} = kr$  as

$$\mathbf{E}(\mathbf{r}, t) = (e^{-i\omega(t-r/c)}) (e^{-i(2\pi\delta/\lambda)r}) (e^{-(2\pi\beta/\lambda)r}). \quad (5.7)$$

The first term in parentheses is the wave propagation, the second term is a phase shift proportional to  $\delta$  that is induced by the dispersive medium, and the third term is a decay in amplitude that is proportional to  $\beta$ . From this relationship, it can be shown that the attenuation of the intensity is given by

$$\frac{I}{I_0} = e^{-(4\pi\beta/\lambda)r} = e^{-n_a\sigma_a r} \quad (5.8)$$

where  $I_0$  is the initial intensity and  $\sigma_a = 2r_\lambda f_2(\omega)$  is the photoabsorption cross section. This relationship shows that by measuring the absorption of a material (a thin, free-standing film for these photon energies), one can easily extract the imaginary part of the refractive index.

The effect of the real part of the refractive index is to induce a phase shift in propagating field, as can be seen from equation 5.7. After propagating through a material of thickness  $L$ , the induced phase shift is given by

$$\Delta\phi = \frac{2\pi\delta L}{\lambda}. \quad (5.9)$$

To experimentally access this phase shift, the technique that can be used is interferometry [35–37]. The idea is to create a Mach-Zehnder interferometer (see figure 5.2), and in one of the arms introduce a sample of thickness  $L$ . By measuring how the interference patterns shift when introducing the sample, then one can directly measure the phase shift induced by the sample. Additionally, by looking at how the fringe contrast changes, one can also get access to the attenuation caused by the sample. This means that both the real and imaginary parts of the refractive index can be probed simultaneously. This concept is precisely what will be used to extract the real and imaginary parts using the two XUV sources generated by a SWPG. In that case each source will act as one arm of a Mach-Zehnder interferometer.

## 5.3 Measurement of the complex refractive index

### 5.3.1 Experimental setup

The experimental setup that will be used to demonstrate the ability to measure both the real and imaginary parts of the refractive index is very similar to the experimental setup presented in chapter 4. The TABLE is the experimental beamline that will be used, and the setup is shown in figure 5.3. We use the output of the TOPAS at 1435 nm with a pulse energy of about 2 mJ and a pulse duration of around 70 fs. A  $0 - \pi$  SWPG with a grating period of 2.5 mm is used to generate two intense lobes at the focal plane of a 400

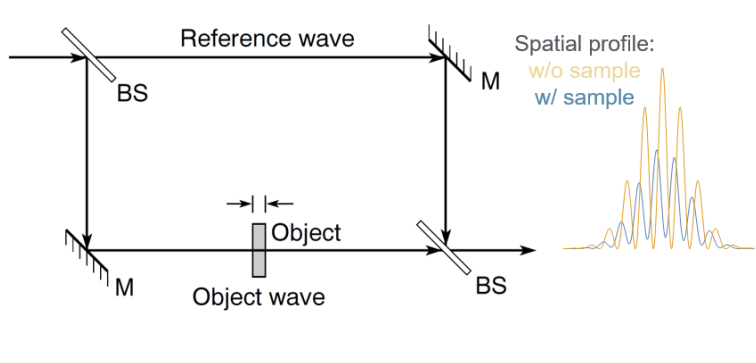


Figure 5.2: Schematic of a Mach-Zehnder interferometer that is used to measure the phase shift induced by a sample placed in one of the arms of the interferometer. For the experiments described in this chapter, the two XUV sources will act as the two arms of a Mach-Zehnder. Modified from [3].

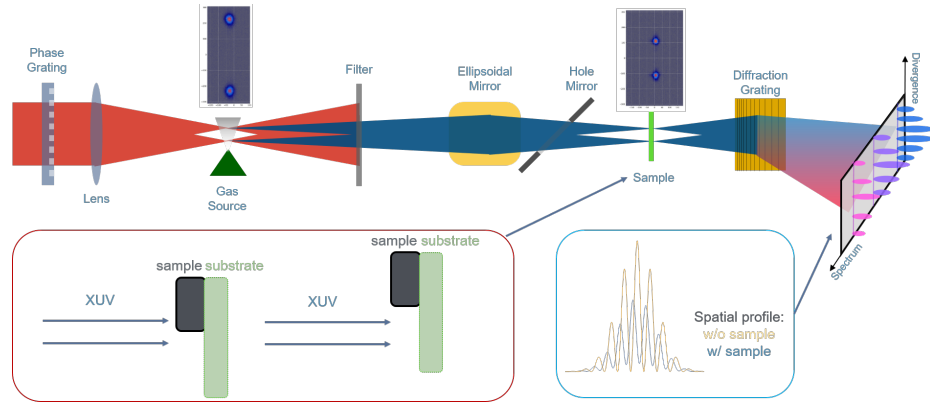


Figure 5.3: Schematic of the two-source HHG experiment performed in the TABLE. A  $0 - \pi$  SWPG is used to generate two intense lobes at the focus of a lens. These lobes will generate XUV beams which will interfere in the far-field. An ellipsoidal mirror is used to refocus the XUV beams into a target chamber before going onto the spectrometer. A sample that is shaped like a step-function will be introduced at the focus of the XUV in the target chamber. The spatial profile of the various harmonic orders will be measured in the two cases shown. The fringe shift and fringe contrast changes allow for a simultaneous measurement of both parts of the refractive index of the sample.

mm focal length CaF<sub>2</sub> plano-convex lens. At the focal plane, a gas medium is generated by a piezoelectric pulsed gas jet in which harmonics will be generated by the two sources. The generation gas that will be used is argon. The fundamental wavelength is then filtered out by an aluminum filter. The Al filter acts a high frequency bandpass with a bandpass region of 20-72 eV for the harmonic energies that are generated at this wavelength. The harmonics are then refocused into a target chamber by an ellipsoidal mirror with a demagnification of three. This entails that the source separation in the target chamber will be smaller by a factor of three, and the beam waist of each source will also be reduced by a factor of three. This is where a sample will be introduced into only one of the two XUV sources. After transmitting through the sample, the XUV will propagate to the spectrometer which allows for the spatial profile of each harmonic order to be measured.

In order to implement the scheme shown in figure 5.3, we need to introduce a sample into only one of the two XUV sources that are generated. As mentioned previously, the source separation in the target chamber will be a third of the separation in the generation chamber. For the SWPG and laser parameters that we used for this experiment, the source separation in the harmonic generation chamber is  $\Delta x = 2\lambda f/d \approx 460 \mu m$ , and the corresponding separation will be  $\Delta x_t = \Delta x/3 \approx 153 \mu m$  in the target chamber. Therefore, the ideal sample has a cross sectional profile that is as close to a step function as possible, and the width of the step should be much less the separation between the two sources. In general, this can be accomplished using photolithography techniques to pattern a thin film on top of a free standing membrane substrate. For the sample that is used in this proof of principle experiment, we instead chose to start with a commercially available free standing membrane, and then break the membrane in such a way that it would have a sharp step-like cross sectional profile. The membrane that was chosen was a free standing 260 nm single crystal Si membrane on a 500  $\mu m$  Si frame. These free standing membranes are manufactured by Norcada. The sample needs to be this thin because this experiment is done in transmission and XUV is strongly absorbed by most materials. A schematic of the sample that was used is shown in figure 5.4.

### 5.3.2 Results

To measure the complex refractive index of the silicon sample shown in figure 5.4, we will look for a fringe shift and change in fringe contrast when only one of the sources is going through the Si sample and the other is going through vacuum. To see this, we translate the sample through the focal plane in the target chamber such that there are three distinct regimes will occur. The first is when both samples are going through vacuum, the second is when one sample is going the sample and the other is going through vacuum, and the final regime is when both samples are going through the Si membrane. Since this is a differential measurement, we would only expect to see a fringe shift for the second regime. The first and

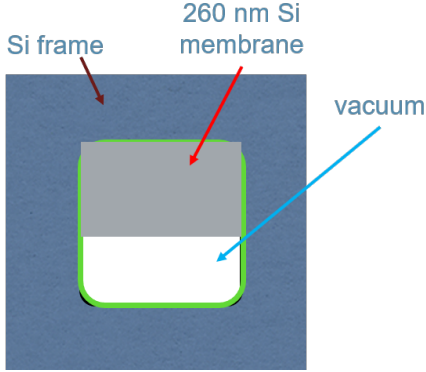


Figure 5.4: Schematic of the sample that was used in this experiment. It is a free standing 260 nm Si membrane that has been broken in half. The way that the sample was cleaved in half ensures that the edge is sharper than the separation between the two sources. The sample was made by Norcada before it was broken.

third regimes should show the same fringe pattern, and the only expected difference is the overall modification of the spectral amplitude of the harmonics that due the absorption of the Si membrane. This is shown in figure 5.5, where the spatial profile is shown for harmonic order 29 as the sample is translated through the focal plane. From the spatial profile shown in figure 5.5, the three expected regimes can clearly be seen. There is also additional spatial structure that is present in the transition between each of the three regimes. This is due to diffraction that is caused by one of the sources being partially blocked. From the spatial profile, the fringe shift can be extracted from the spatial frequency component that corresponds to this harmonic. The phase of that spatial frequency is plotted in 5.5 and shows that there is a phase shift between the two sources when only one of the sources is going the sample. From this phase shift it is now possible to calculate the real part of the refractive index from the relationship  $\Delta\phi = 2\pi\delta L/\lambda$  where  $\Delta\phi$  is the phase shift between the two sources. The phase shift that is observed in harmonic order 29 can be seen across the harmonic spectrum, and enables the real part of the refractive index to be extracted across a broad range of photon energies simultaneously.

In addition to the fringe shift that is show in figure 5.5, there is also a change in fringe contrast that can be seen as the sample is translated through the two sources. In general, the fringe contrast can be defined as the relative difference of of the maximum and minimum values of an interference pattern, such that

$$V = \frac{I_{max} - I_{min}}{I_{max} + I_{min}} \quad (5.10)$$

is the fringe visibility or contrast. When considering the case of two interfering beams, this

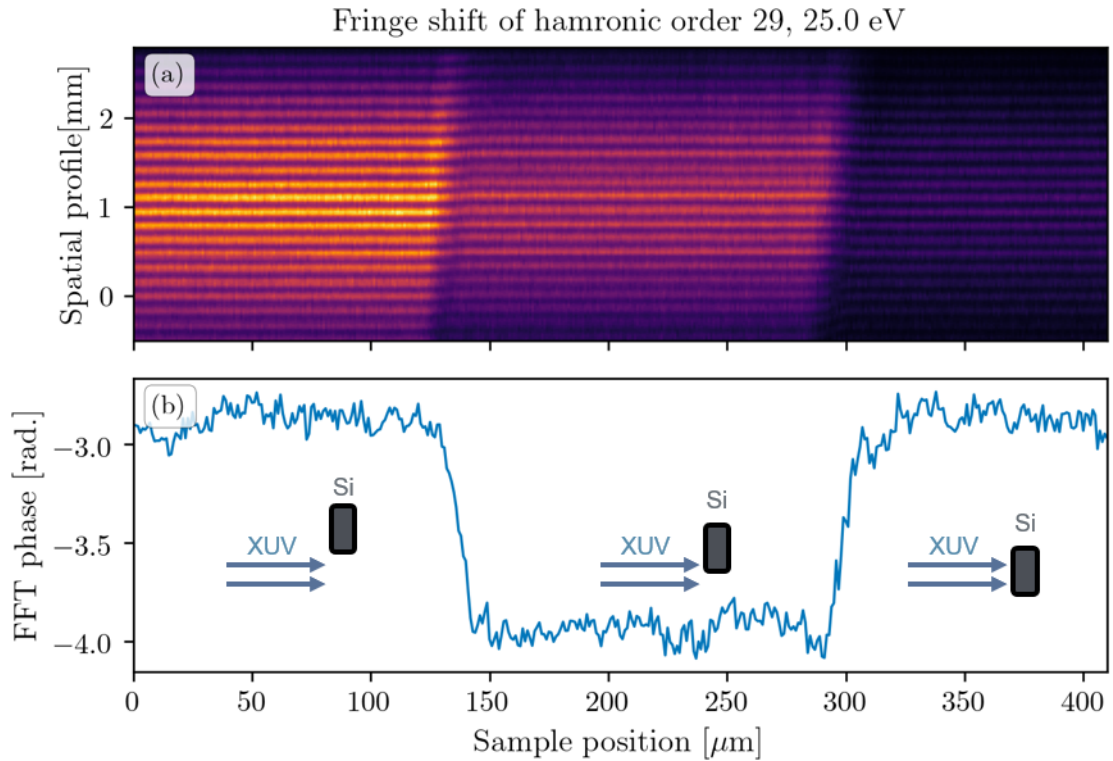


Figure 5.5: (a) Spatial profile of harmonic order 29 as the silicon sample is translated through the two sources. Three regimes are clear from the spatial profile, and they correspond to both sources going through vacuum, only one source going through the sample, and both sources going through the sample. A clear fringe shift can be seen between the second regime and the other two. Additional structure is seen at the transition between regimes, and this is due to diffraction cause by the sample partially blocking one of the sources. (b) Phase extracted from the spatial frequency corresponding to this harmonic order. The phase shift induced by the Si sample can be extracted from this phase shift.

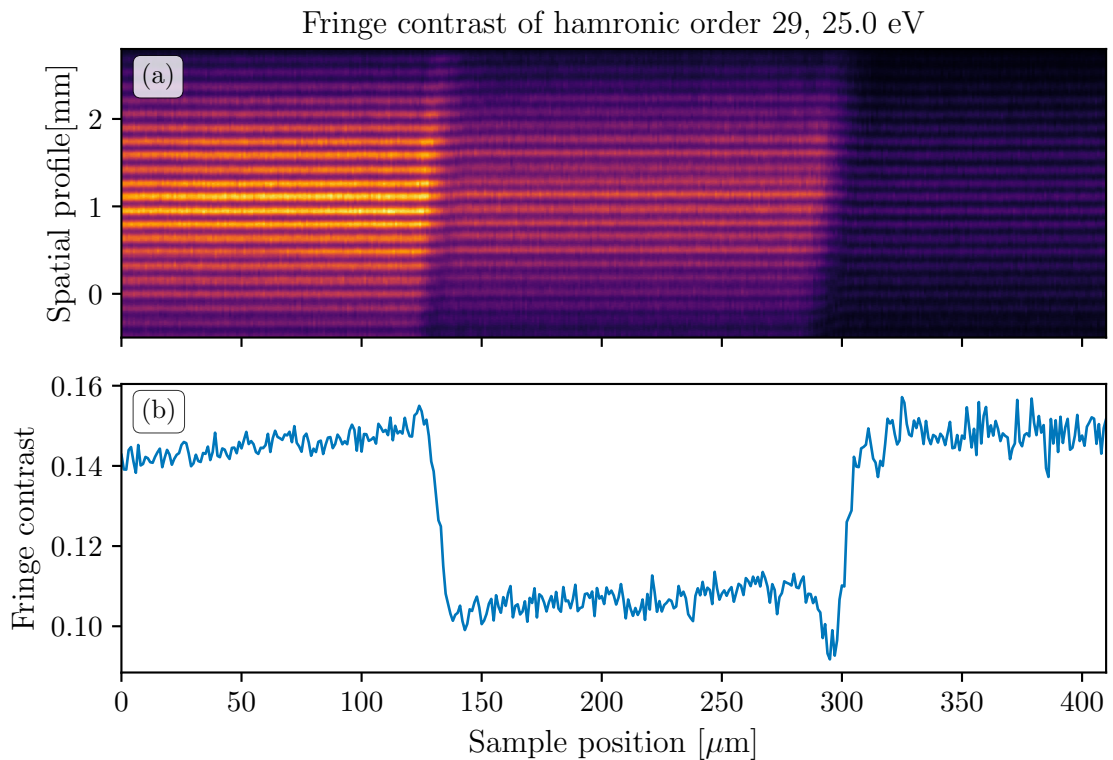


Figure 5.6: (a) Spatial profile of harmonic order 29 as the silicon sample is translated through the two sources. Three regimes are clear from the spatial profile, and they correspond to both sources going through vacuum, only one source going through the sample, and both sources going through the sample. (b) Fringe contrast extracted from the spatial frequency corresponding to this harmonic order.

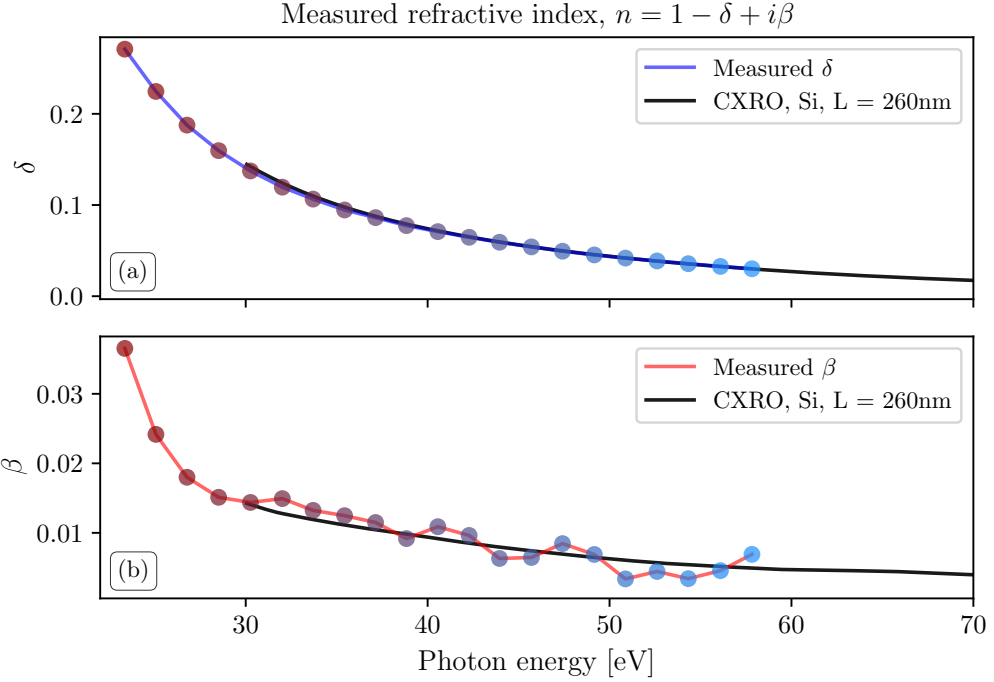


Figure 5.7: (a) Real part of the refractive index measured using a SWPG. Shows excellent agreement with the values from CXRO. (b) Imaginary part of the refractive index measured using a SWPG. Shows excellent agreement with the values obtained from CXRO.

fringe contrast can be written as

$$V = \frac{2\sqrt{I_1 I_2}}{I_1 + I_2} \gamma_{12} \quad (5.11)$$

where  $I_1$  and  $I_2$  are the intensity of the two beams and  $\gamma_{12}$  is the coherence between them [36–38]. This change in fringe contrast is shown in figure 5.6. The contrast shows the three distinct regimes that were seen in the fringe shift. Similarly to the fringe shift, it can be seen that there is only a change in fringe contrast when only one of the sources is going through the sample. From this contrast, it is possible to calculate the imaginary part of the refractive index. This can be done using the relationship

$$\beta = -\frac{\lambda}{2\pi L} \ln \left[ \frac{V_0}{V} \left( 1 - \sqrt{1 - \left( \frac{V}{V_0} \right)^2} \right) \right] \quad (5.12)$$

where  $V_0$  is the contrast with the sample and  $V$  is the contrast with the sample present in one of the sources [36].

By combining both the fringe shift and the change in fringe contrast, we can now calculate both the real and imaginary part of the refractive index of Si over the range

25 - 60 eV. The results are shown in figure 5.7. As can be seen in the figure, there is excellent agreement between the measured real and imaginary part when compared to the values that can be obtained from CXRO [39].

## 5.4 Conclusion

In this chapter, the complex refractive index was introduced and a method to measure both the real and imaginary parts was proposed. The method relies on the use of a  $0-\pi$  SWPG to generate two relative phase locked XUV sources whose interference acts as an inline Mach-Zehnder interferometer. By introducing a sample into one of the sources, the corresponding fringe shift and change in fringe contrast gives access to the real and imaginary parts of the refractive index. A sample of Si was fabricated to test this method, and measuring it's refractive index shows excellent agreement between our measured results and the literature. By demonstrating that it is possible to accurately extract both the real and imaginary parts, we have accurately characterized the ground state of a condensed matter system. The next step is to extract the dynamic real and imaginary parts that are induced by dressing the sample with another IR field. This will be discussed in a later chapter.

# Chapter 6

## ATTOSECOND TRANSIENT-ABSORPTION SPECTROSCOPY

### 6.1 Introduction

### 6.2 Theory

### 6.3 Autoionization resonances

One of the most extensively studied phenomena using ATS has been autoionization of noble gas atoms in the time-domain [40–44]. Autoionization was first observed in 1935 by Beutler [45] by studying photoabsorption of noble gas atoms, and it manifested itself as sharp, asymmetric peaks in the absorption spectrum. These features were theoretically described by Fano in a seminal paper in 1961 [4, 46] as the result of interference between two pathways: direct ionization to the continuum and autoionization from a discrete state that is embedded in and coupled to the continuum. The theoretical framework that he developed can be treated as a more general formalism that describes interference between discrete and continuous pathways.<sup>1</sup> For this very reason, "Fano" resonances can be observed in a plethora of atomic, molecular, and condensed matter systems [50].

#### 6.3.1 Time-independent autoionization: Fano's original work

As noted above, Fano's theoretical explanation of the photoabsorption spectrum observed by Beutler in noble gas atoms is based on interference between two pathways. The relevant level diagram to describe this scenario is shown in figure 6.1, and specifically we will be considering the autoionization resonances in Ar because they will be used in the ATS experiments described in this chapter and in the following chapter. In this case, there is a

<sup>1</sup>A very similar theory was independently developed by Feshbach in the context of nuclear physics, and these two theories have been unified by further theoretical work [47–49].

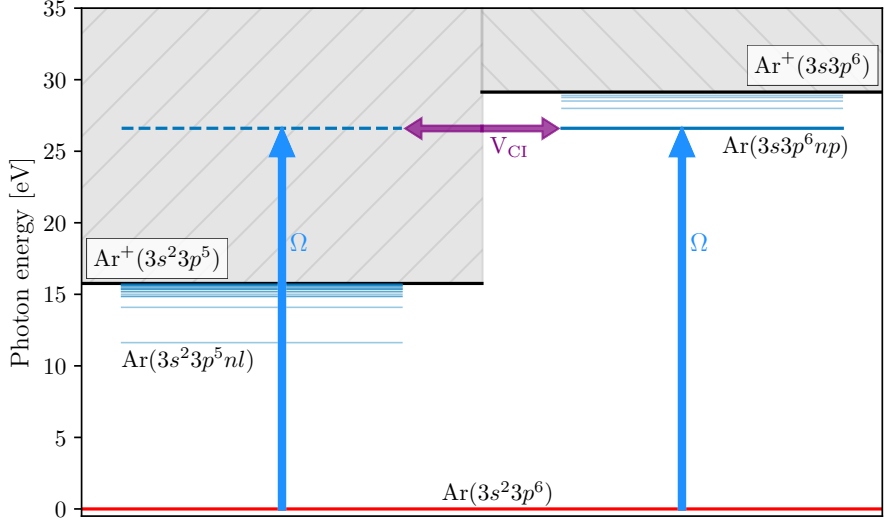


Figure 6.1: Level diagram of argon showing the effect of autionization states on XUV photoabsorption. There are two possible pathways for ionization with a photon of energy  $\Omega$ : (1) direct ionization to a continuum state (left side of figure) and (2) excitation to a bound state in the continuum (right side of figure). In case (2), there is coupling between the bound state and the continuum through the configuration interaction. This allows for the bound state to decay to the same continuum state as in case (1). These effect leads to interference between these two pathways.

bound state  $|\psi_b\rangle$  (one of the  $3s3p^6np$  states in Ar) that is embedded within a set of continuum states  $|\psi_\varepsilon\rangle$ . This entails that the energy of the bound state  $E_b$  is degenerate with the energetic spectrum of continuum states. The coupling between the bound state  $|\psi_b\rangle$  and the continuum  $|\psi_\varepsilon\rangle$  through the configuration interaction leads to decay of the electron from the bound state to the continuum. The following derivation of the photoabsorption cross section and phase follows closely from Fano's original paper and sources that have reproduced his original derivation [4, 41, 51].

The Hamiltonian describing this system can be written as

$$\hat{H} = \hat{H}_0 + \hat{V}, \quad (6.1)$$

where  $\hat{H}_0$  is the zeroth order Hamiltonian and  $\hat{V}$  is the correlation potential that describes the coupling between the discrete state  $|\psi_b\rangle$  and the continuum state  $|\psi_\varepsilon\rangle$ . The solutions to the zeroth order Hamiltonian are the continuum and bound states, such that

$$\hat{H}_0 |\psi_b\rangle = E_b |\psi_b\rangle \quad (6.2)$$

$$\hat{H}_0 |\psi_\varepsilon\rangle = \varepsilon |\psi_\varepsilon\rangle \quad (6.3)$$

where the states  $|\psi_b\rangle$  and  $|\psi_\varepsilon\rangle$  are orthonormal. These two solutions to the zeroth order Hamiltonian are referred to as configurations, and the interaction between them is given by  $\hat{V}$ . The coupling strength between these two configurations is given by the off-diagonal matrix element  $V_\varepsilon$ , such that

$$\langle\psi_\varepsilon|\hat{H}|\psi_b\rangle = \langle\psi_\varepsilon|\hat{H}_0 + \hat{V}|\psi_b\rangle = \langle\psi_\varepsilon|\hat{V}|\psi_b\rangle = V_\varepsilon. \quad (6.4)$$

This configuration interaction matrix element  $V_\varepsilon$  depends upon the energy  $\varepsilon$  and is generally a smooth function of the continuous energy  $\varepsilon$ . Furthermore, the configuration interaction only couples different configurations and not within the same configuration. This means that the diagonal matrix elements of  $\hat{V}$  are zero,

$$\langle\psi_\varepsilon|\hat{V}|\psi_\varepsilon\rangle = 0 \quad (6.5)$$

$$\langle\psi_b|\hat{V}|\psi_b\rangle = 0. \quad (6.6)$$

Therefore, the diagonal matrix elements of the full Hamiltonian in equation 6.1 are given by

$$\langle\psi_\varepsilon|\hat{H}|\psi_\varepsilon\rangle = \varepsilon\delta(\varepsilon - \varepsilon') \quad (6.7)$$

$$\langle\psi_b|\hat{H}|\psi_b\rangle = E_b. \quad (6.8)$$

Armed with these states as a basis, we can now expand an eigenstate of the full Hamiltonian  $\hat{H}$ . This entails that the eigenstate  $|\Psi_E\rangle$  of energy  $E$ , which is found by solving the equation

$$\hat{H}|\Psi_E\rangle = E|\Psi_E\rangle, \quad (6.9)$$

can be expanded in this complete basis, such that

$$|\Psi_E\rangle = a(E)|\psi_b\rangle + \int d\varepsilon' b(\varepsilon', E)|\psi_\varepsilon'\rangle. \quad (6.10)$$

The physical interpretation of this expansion is that an electron at energy  $E$  can originate from either the discrete state  $|\psi_b\rangle$  or from the continuous state  $|\psi_\varepsilon\rangle$ . The contribution from  $|\psi_\varepsilon\rangle$  is direct ionization, and the contribution from  $|\psi_b\rangle$  is autoionization (i.e. decay from the bound state  $|\psi_b\rangle$  to the continuum). The relative contributions of these two channels is given by the expansion coefficients  $a(E)$  and  $b(\varepsilon, E)$ .

These expansion coefficients can be solved for and it involves algebra that is described in full detail in Fano's paper [4]. The first step is to evaluate the relationship

$$\langle\Psi_E|\hat{H}|\Psi_E\rangle = E \quad (6.11)$$

using the expansion in eqn. 6.10. This results in a system of two equations with the

unknown coefficients  $a(E)$  and  $b(\varepsilon, E)$ . This system can be solved for analytical expressions of the expansion coefficients, and they are given by

$$a(E) = \frac{\sin \Delta(E)}{\pi V_E} \quad (6.12)$$

$$b(\varepsilon', E) = \frac{V_{\varepsilon'}}{E - \varepsilon'} a(E) - \delta(\varepsilon' - E) \cos \Delta(E) \quad (6.13)$$

where

$$\Delta(E) = -\arctan \left( \frac{\pi |V_E|^2}{E - E_b - F(E)} \right) \quad (6.14)$$

$$F(E) = \text{PV} \int d\varepsilon' \frac{|V_{\varepsilon'}|^2}{E - \varepsilon'} \quad (6.15)$$

and PV is the Cauchy principal value. The term  $F(E)$  is an energy-dependent shift of the bound state that depends upon the strength of the configuration interaction  $|V_{\varepsilon'}|^2$ . This shift can be either positive or negative, depending upon the sign of  $\partial_{\varepsilon'}|V_{\varepsilon'}|^2$  at  $\varepsilon' = E$ , where  $\partial_{\varepsilon'}$  is the partial derivative with respect to  $\varepsilon'$ . Thus, any change in  $V_{\varepsilon'}$  by an external field will lead to a shift in the resonance position.

Substituting the coefficients in equations 6.12 and 6.13 into equation 6.10 yields

$$|\Psi_E\rangle = \frac{\sin \Delta(E)}{\pi V_E} |\psi_b\rangle + \frac{\sin \Delta(E)}{\pi V_E} \left( \text{PV} \int d\varepsilon' \frac{V_{\varepsilon'}}{E - \varepsilon'} \right) |\psi'_{\varepsilon'}\rangle - \cos \Delta(E) |\psi_E\rangle. \quad (6.16)$$

This can be further simplified by introducing a modified discrete state given by

$$|\Phi\rangle = |\psi_b\rangle + \text{PV} \int d\varepsilon' \frac{V'_{\varepsilon'}}{E - \varepsilon'} |\psi'_{\varepsilon'}\rangle, \quad (6.17)$$

which allows us to express the eigenstate  $|\Psi_E\rangle$  as

$$|\Psi_E\rangle = \frac{\sin \Delta(E)}{\pi V_E} |\Phi\rangle - \cos \Delta(E) |\psi_E\rangle. \quad (6.18)$$

Finally, the argument of equation 6.15 can be written in terms of an important parameter, the reduced energy given by

$$\epsilon = \frac{E - (E_b + F(E))}{\Gamma(E)/2} = \frac{E - E_{\Phi}}{\Gamma/2} \quad (6.19)$$

where

$$\Gamma(E) = 2\pi|V_E|^2 \approx \Gamma(E_b) = \Gamma. \quad (6.20)$$

The interpretation of the modified bound state  $|\Phi\rangle$  is that the configuration interaction is mixing the original discrete state  $|\psi_b\rangle$  and the continuum states  $|\psi'_{\varepsilon'}\rangle$ . So, for an energetic window near  $E = E_{\Phi}$ , one can consider the resonance energy to be  $E_b$  and the resonance linewidth to be  $\Gamma$ . Since  $\Gamma = 2\pi|V_E|^2$ , the resonance linewidth and the natural lifetime  $h/\Gamma$

are directly related to the strength of the coupling between bound states and continuum states through the configuration interaction. Therefore, stronger (weaker) coupling would lead to faster (slower) decay from bound to continuum states, respectively. From this, it can be seen that an external field that is able to modify the strength of the configuration interaction, then that will lead to a change in the linewidth and position of the resonance.

Now that the eigenstates of the Hamiltonian  $\hat{H}$  have been expanded, we will turn our attention to the photoabsorption spectrum. In the original experiments done by Beutler, a sharp, asymmetric absorption profile was seen in the photoabsorption spectrum of noble gas atoms in the XUV [45]. From the expanded eigenstate given in equation 6.18, we can begin see how this asymmetric absorption profile might arise. The coefficients in the expansion are proportional to sine and cosine functions of the reduced energy  $\epsilon$ , and, since they are odd and even functions of  $\epsilon$ , this will lead to constructive and destructive interference on either side of the resonance. It is precisely this effect that will give rise to the asymmetric absorption lineshape.

To derive the photoabsorption spectrum, we will consider a transition from the ground state of the atom  $|g\rangle$  by a XUV photon of energy  $\Omega$ . This can be described through the use of the dipole transition operator

$$\hat{D} = -e\hat{\mathbf{r}} \cdot \mathbf{E}_{XUV}(t) \quad (6.21)$$

where  $\mathbf{E}_{XUV}(t)$  is the electric field of the XUV. Using this operator, the transition probability is given by the matrix element

$$\begin{aligned} \langle \Psi_E | \hat{D} | g \rangle &= \frac{1}{\pi V_E^*} \sin \Delta(E) \langle \Phi | \hat{D} | g \rangle - \cos \Delta(E) \langle \psi_E | \hat{D} | g \rangle \\ &= \cos \Delta(E) \langle \psi_E | \hat{D} | g \rangle \left[ \tan \Delta(E) \frac{1}{\pi V_E^*} \frac{\langle \Phi | \hat{D} | g \rangle}{\langle \psi_E | \hat{D} | g \rangle} - 1 \right]. \end{aligned} \quad (6.22)$$

At this point, we can now introduce the well-known and important  $q$  parameter, given by

$$q(E) = \frac{1}{\pi V_E^*} \frac{\langle \Phi | \hat{D} | g \rangle}{\langle \psi_E | \hat{D} | g \rangle} \approx q(E_b) = q. \quad (6.23)$$

The  $q$  parameter describes the asymmetry of the resonance, and it is related to the ratio of transitions to the modified bound state  $|\Phi\rangle$  and the continuum states  $|\psi_E\rangle$ . Combining equations 6.22, 6.23, and 6.14, we arrive at

$$\langle \Psi_E | \hat{D} | g \rangle = -\cos \Delta(E) \langle \psi_E | \hat{D} | g \rangle \left[ \frac{\pi |V_E|^2}{E - (E_b + F(E))} q + 1 \right] \quad (6.24)$$

$$= -\cos \Delta(E) \langle \psi_E | \hat{D} | g \rangle \left[ \frac{\Gamma/2}{E - (E_b + F(E))} q + 1 \right], \quad (6.25)$$

	$\Delta E$ [eV]	$\Gamma$ [meV]	$q$	$\rho^2$
$3s3p^64p$	26.605	80.2(7)	-0.286(4)	0.840(3)
$3s3p^65p$	27.994	28.5(8)	-0.177(3)	0.848(3)
$3s3p^66p$	28.509	12.2(3)	-0.135(9)	0.852(9)
$3s3p^67p$	28.757	6.6(1)	-0.125(4)	0.846(9)
$3s3p^68p$	28.898	4.5(2)	-0.132(4)	0.77(2)

Table 6.1: Parameters of the  $3s3p^6np$  Fano resonances in argon. These values were extracted from experimental cross sections, see [5–7].

and this can be further simplified using the reduced energy  $\epsilon$ , which yields

$$\langle \Psi_E | \hat{D} | g \rangle = - \langle \psi_E | \hat{D} | g \rangle \cos \Delta(E) \left( \frac{q}{\epsilon} + 1 \right) \quad (6.26)$$

$$\langle \Psi_E | \hat{D} | g \rangle = \langle \psi_E | \hat{D} | g \rangle \frac{q + \epsilon}{\epsilon + i}. \quad (6.27)$$

Finally, using this relationship the ratio of transition probabilities can be calculated and leads to the well known Fano lineshape,

$$\frac{|\langle \Psi_E | \hat{D} | g \rangle|^2}{|\langle \psi_E | \hat{D} | g \rangle|^2} = \frac{(q + \epsilon)^2}{\epsilon^2 + 1}. \quad (6.28)$$

This ratio is proportional to the photoabsorption cross section, and is plotted for various  $q$  parameters in figure 6.2. As can be seen, the lineshape's symmetry dramatically depends upon the  $q$  parameter, and the cross section even goes to zero at different energies, depending upon  $q$ . This is a direct consequence of the destructive interference from the configuration states, as was predicted earlier in the derivation. Additionally, the spectral phase of the Fano profile can also be extracted, given by

$$\theta(\epsilon) = \arg \left[ \frac{q + \epsilon}{\epsilon + i} \right], \quad (6.29)$$

and is plotted in figure 6.2 (b). For increasing  $\epsilon$ , the phase increases until  $\epsilon = -q$  when there is a  $\pi$  phase jump, and thereafter the phase continues to increase until it asymptotically approaches its original value.

Experimentally the photoabsorption cross section is generally fit to the form

$$\sigma_{\text{PCS}} = \sigma_a \frac{(q + \epsilon)^2}{\epsilon^2 + 1} + \sigma_{NR} \quad (6.30)$$

where  $\sigma_a$  scales the strength of the Fano profile and  $\sigma_{NR}$  is a non-resonant cross section that is included to account for absorption from other continuum states that might be present.

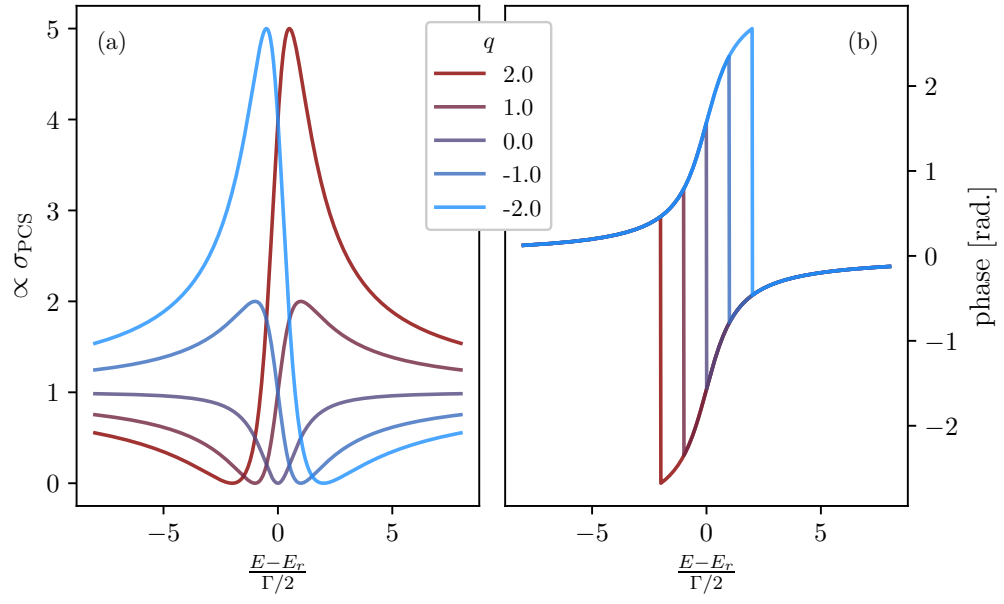


Figure 6.2: (a) Calculation of the photoabsorption cross section near a resonance for the listed  $q$  parameters. The change from symmetric to asymmetric profiles can be seen as the  $q$  parameter is varied. Maximum and minimum in cross section occurs at  $\epsilon = 1/q$  and  $\epsilon = -q\Gamma^2/4$ , respectively. (b) Calculation of the phase across the resonance for different  $q$  parameter. The  $\pi$  phase jump clearly depends on  $q$ , and it occurs when  $\epsilon = -q$  and not at the resonance energy  $E_r$ . Calculations based on U. Fano's original work [4].

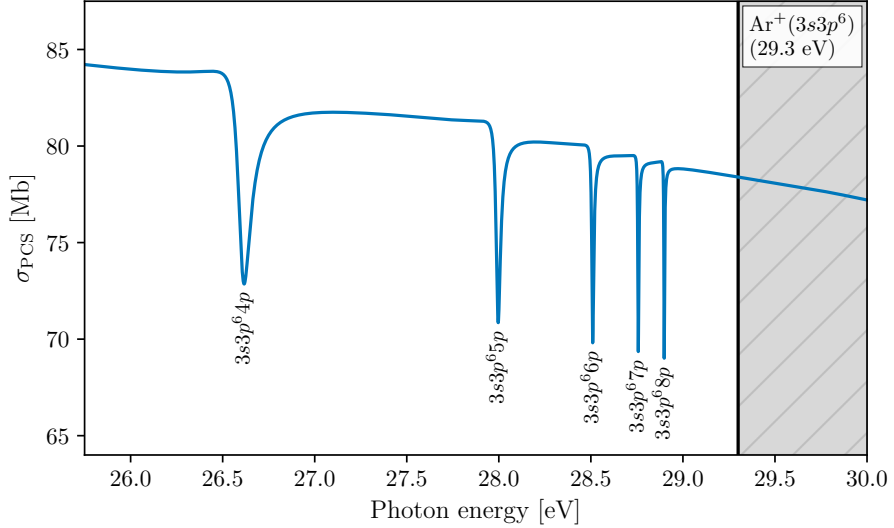


Figure 6.3: Photoabsorption cross section of the Argon  $3s3p^6np$  Fano resonances (blue curve), with only resonances up to  $n = 8$  shown. Grey shaded area indicates the energetic region above the  $\text{Ar}^+(3s3p^6)$  ionization threshold. Values used to calculate this cross section are shown in Table 6.1.

### 6.3.2 Time-dependent autoionization

Up until this point, Fano resonances have been discussed in a time-independent manner in the frequency domain. However, one would ideally like to describe these autoionizing resonances in the time domain, as that will lend itself to the experiments described herein. This description was primarily done by W.-C. Chu and C.D. Lin [52], and it has been used to interpret many ATS experiments [42, 43, 53, 54]. The basic assumption that is made in this treatment is that the XUV pulse that excites from the ground state to the Fano resonance is a Dirac- $\delta$  function in time,  $\mathbf{E}_{XUV} = E_0\delta(t)\mathbf{z}$ . This impulsive excitation is generally a reasonable approximation for an attosecond XUV pulse that is shorter in duration than the typical lifetimes of these resonances. From this assumption, it is possible to analytically describe the dipole response of the system in the time domain.

The derivation of the dipole response follows naturally from the theory described in the previous section. Assuming that the XUV impulsively excites at  $t = 0$  from the ground state  $|g\rangle$  to the bound and continuum states  $|\psi_b\rangle$  and  $|\psi_\varepsilon\rangle$ , the wave function for times  $t > 0$  can be in the configuration states, such that

$$|\Psi(t)\rangle = e^{-i\varepsilon_g t} |g\rangle + c_b(t) |\psi_b\rangle + \int c_\varepsilon(t) |\psi_\varepsilon\rangle d\varepsilon. \quad (6.31)$$

Since the configuration states  $|\psi_b\rangle$  and  $|\psi_\varepsilon\rangle$  are not eigenstates of the total Hamiltonian, the expansion coefficients  $c_b$  and  $c_\varepsilon$  are explicitly time dependent. The evolution of these coefficients is governed by the Time-Dependent Schrödinger Equation (TDSE)

$$i\frac{\partial}{\partial t} |\Psi(t)\rangle = \hat{H} |\Psi(t)\rangle, \quad (6.32)$$

and using this equation, the time dependence of the expansion coefficients can be expressed as the coupled differential equations given by

$$\begin{aligned} \frac{\partial c_\varepsilon}{\partial t} &= -iV_\varepsilon c_b(t) - i\varepsilon c_\varepsilon(t) \\ \frac{\partial c_b}{\partial t} &= -i\varepsilon_r c_b(t) - iV_\varepsilon \int c_\varepsilon(t) d\varepsilon. \end{aligned} \quad (6.33)$$

Assuming the initial values  $c_b^{(0)}$  and  $c_\varepsilon^{(0)}$  are known, then the solutions to equations 6.33 are given by

$$\begin{aligned} c_b(t) &= c_b^{(0)} \left( 1 - \frac{i}{q} \right) e^{-i\varepsilon_r t} e^{-\frac{\Gamma}{2}t} \\ c_\varepsilon(t) &= \frac{c_\varepsilon^{(0)}}{\epsilon + i} e^{-i\varepsilon_r t} \left[ (q + \epsilon) e^{-i(E-E_r)t} - (q - i) e^{-\frac{\Gamma}{2}t} \right], \end{aligned} \quad (6.34)$$

where, as in the previous section,  $q = c_b^{(0)} / (\pi V c_\varepsilon^{(0)})$ ,  $\Gamma = 2\pi|V|^2$ , and  $\epsilon = (\varepsilon - \varepsilon_r)/(\Gamma/2)$ .

With the time dependent wave function now in hand, the induced dipole  $d(t)$  can now

be calculated for  $t > 0$  by evaluating  $d(t) = \langle \Psi(t)|z|\Psi(t)\rangle$ . Using equations 6.31 and 6.34, this gives

$$\begin{aligned} d(t) &= c_b(t)e^{-i\varepsilon_g t} \langle \psi_b|z|g\rangle^* + \int c_\varepsilon(t)e^{i\varepsilon_g t} \langle \psi_\varepsilon|z|g\rangle^* + c.c. \\ &= c_b^{(0)} \langle \psi_b|z|g\rangle^* e^{-i\Omega_r t} \left[ \left(1 - \frac{i}{q}\right) e^{-\frac{\Gamma}{2}t} + \frac{1}{(\pi V q)^2} \int \frac{(q+\epsilon)e^{-i\frac{\Gamma}{2}\epsilon t} - (q-i)e^{\frac{\Gamma}{2}t}}{\epsilon+i} d\epsilon \right] + c.c., \end{aligned} \quad (6.35)$$

where  $\Omega_r = E_r - E_g$  is the resonance photon energy. The complex conjugate term in equation 6.35 is a counter-rotating term, and by invoking the rotating wave approximation, it can be dropped. Equation 6.35 can further be evaluated to give

$$\begin{aligned} d(t) &= c_b^{(0)} \langle \psi_b|z|g\rangle^* e^{-i\Omega_r t} \frac{1}{q^2} \left[ q(q-i)e^{-\frac{\Gamma}{2}t} + \frac{2}{\pi\Gamma} \int \frac{(q+\epsilon)e^{-i\frac{\Gamma}{2}\epsilon t} - (q-i)e^{\frac{\Gamma}{2}t}}{\epsilon+i} d\epsilon \right] \\ &= c_b^{(0)} \langle \psi_b|z|g\rangle^* e^{-i\Omega_r t} \frac{1}{q^2} \left[ q(q-i)e^{-\frac{\Gamma}{2}t} + \frac{1}{\pi} \int e^{-i\frac{\Gamma}{2}\epsilon t} d\epsilon + \frac{q-i}{\pi} \int \frac{e^{-i\frac{\Gamma}{2}\epsilon t} - e^{-\frac{\Gamma}{2}t}}{\epsilon+i} d\epsilon \right] \\ &= c_b^{(0)} \langle \psi_b|z|g\rangle^* e^{-i\Omega_r t} \frac{1}{q^2} \left[ q(q-i)e^{-\frac{\Gamma}{2}t} + \frac{4}{\Gamma} \delta(t) + \frac{q-i}{\pi} e^{-\frac{\Gamma}{2}t} 2\pi i + \frac{q-i}{\pi} e^{-\frac{\Gamma}{2}t} \pi i \right] \\ &= c_b^{(0)} \langle \psi_b|z|g\rangle^* \frac{1}{q^2} \left[ \frac{4}{\Gamma} \delta(t) + (q-i)^2 e^{-i\Omega_r t} e^{-\frac{\Gamma}{2}t} \right]. \end{aligned} \quad (6.36)$$

If we assume that  $\langle \psi_b|z|g\rangle$  is real and the expansion coefficient is  $c_b^{(0)}$  purely imaginary, then we can finally arrive at the form of the dipole that is reported in [52, 53, 55],

$$d(t) \propto i \left[ 2\delta(t) + \frac{\Gamma}{2} (q-i)^2 e^{-i\Omega_r t} e^{\frac{\Gamma}{2}t} \right]. \quad (6.37)$$

### 6.3.3 Dipole Control Model

## 6.4 Strong-field Transient Absorption in Argon

### 6.4.1 Experimental setup

### 6.4.2 Results

## 6.5 Conclusion

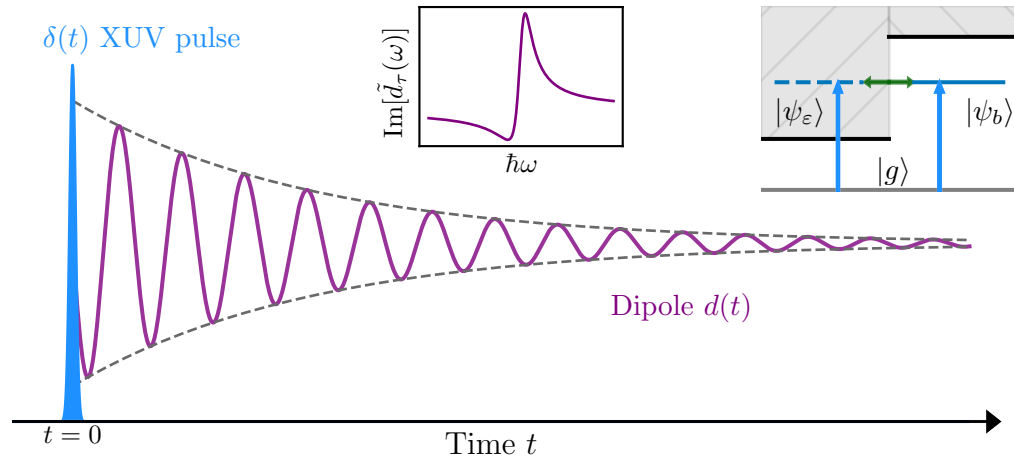


Figure 6.4: Incomplete

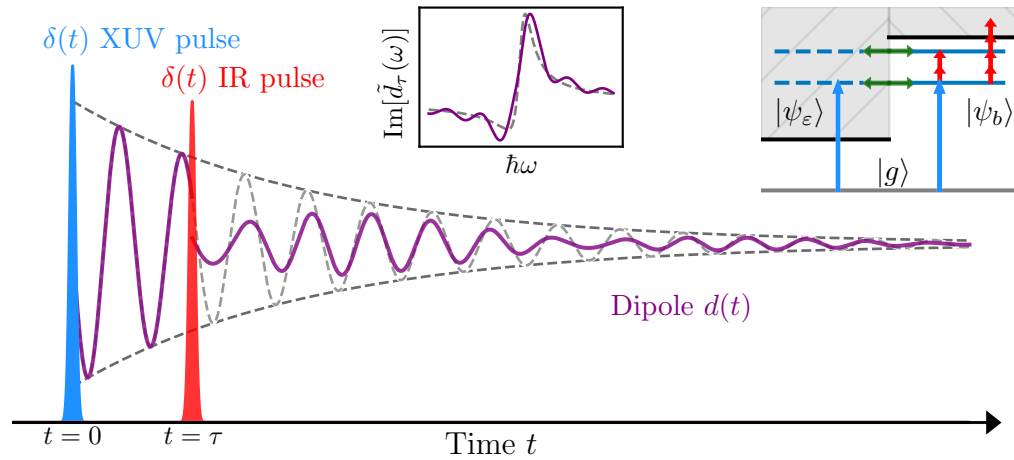


Figure 6.5: Incomplete

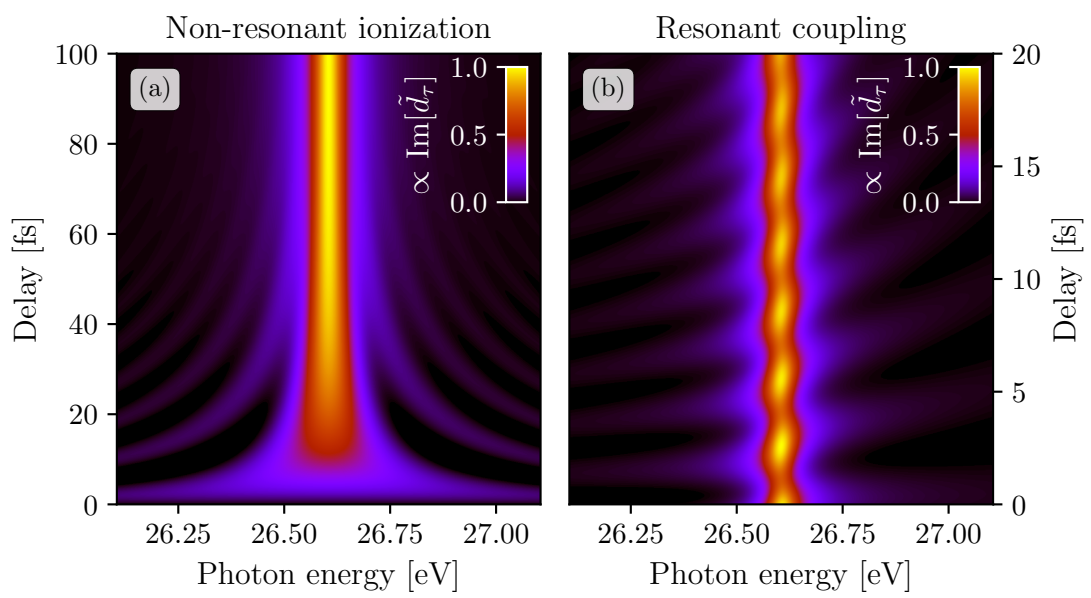


Figure 6.6: Incomplete

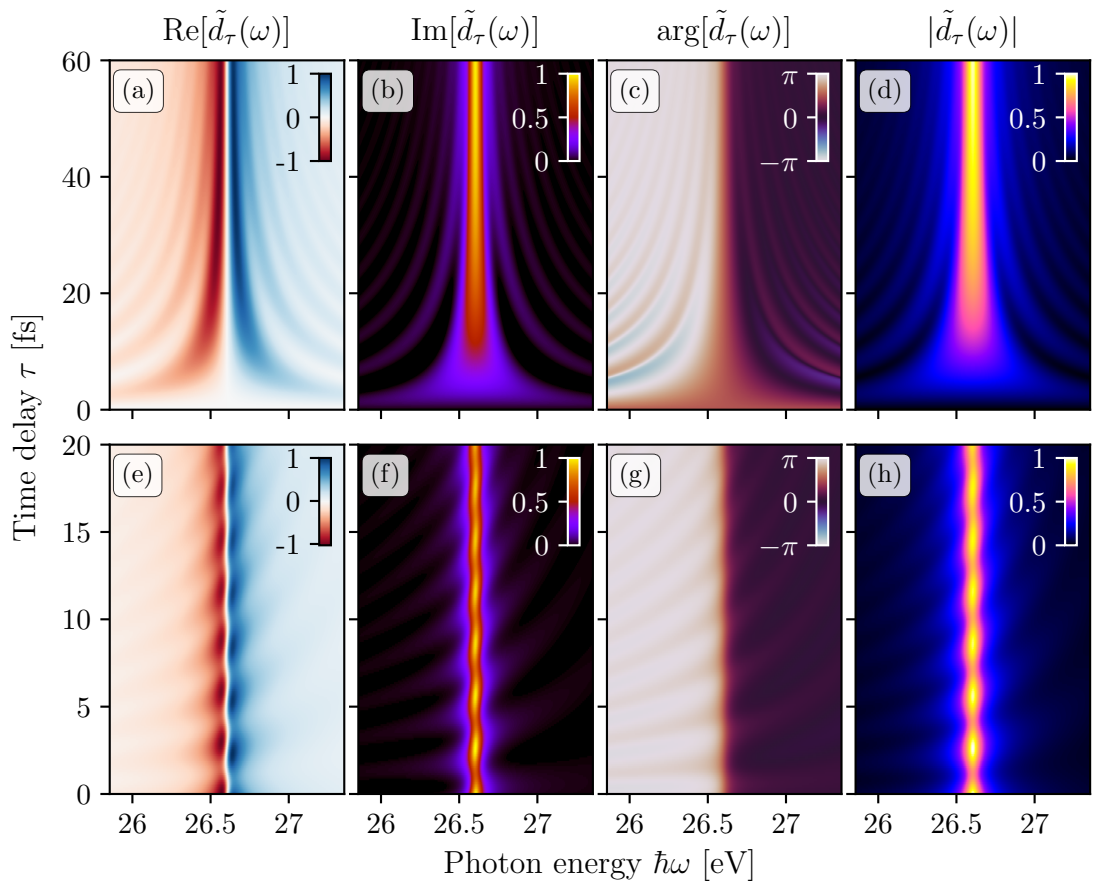


Figure 6.7:  $\varphi_1 = 0$

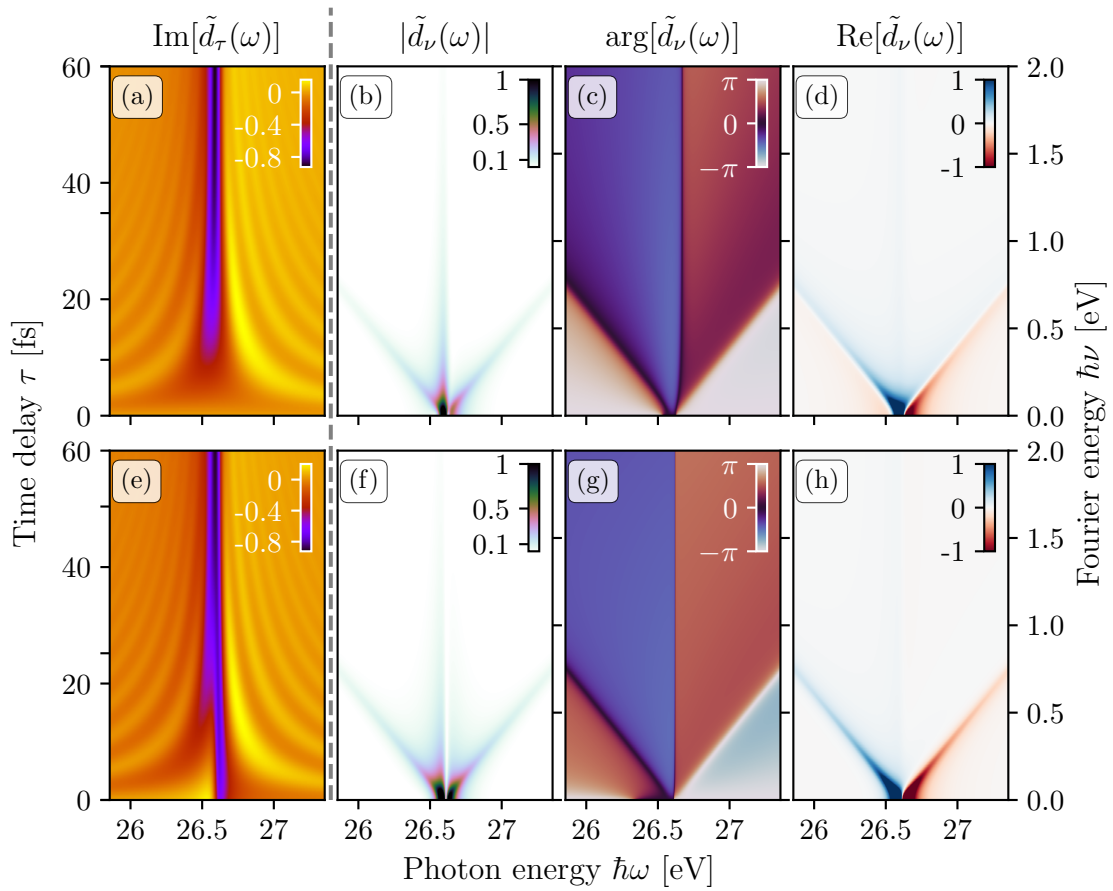


Figure 6.8:  $\phi_0 = 4p$   $a_1 = 0$ ,  $\phi_1 = 0$ ,  $a_1 = 0.8$ ,  $\phi_1 = \pi/2$

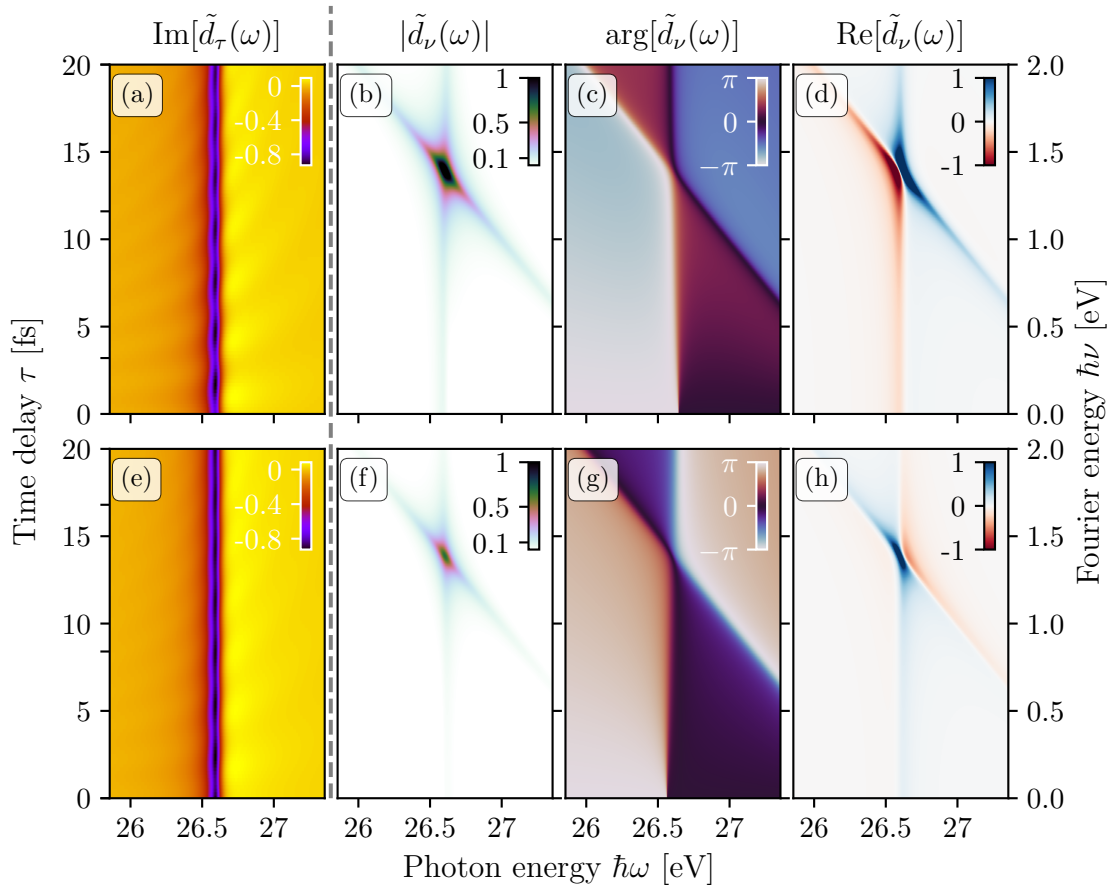


Figure 6.9:  $\phi_0 = 4p$   $a_1 = 0$ ,  $\phi_1 = 0$ ,  $a_1 = 0.8$ ,  $\phi_1 = \pi/2$

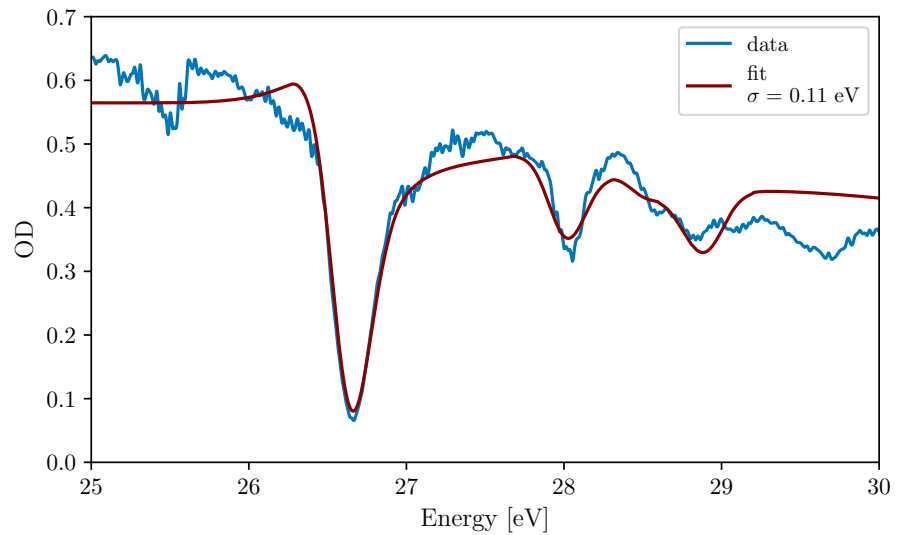


Figure 6.10: Incomplete

# Chapter 7

## COMPLEX ATTOSECOND TRANSIENT-ABSORPTION SPECTROSCOPY

**7.1 Introduction**

**7.2 Theory**

**7.3 Complex Attosecond Transient-absorption Spectroscopy  
of Fano resonances**

**7.3.1 Experimental setup**

**7.3.2 Results**

**7.4 Conculsion**

# Chapter 8

## CONCLUSION

# Appendix A

## SQUARE-WAVE PHASE GRATING

$$I_{IR} = a + b \times \cos(\phi(x_0)) \quad (A.1)$$

$$I_q = \alpha_q \times a^q \left( 1 + N_q \frac{b}{a} \cos(\phi(x_0)) \right) + o(b \times a^{q-1})$$

$$\begin{aligned} I_{IR}(\tilde{x}_1, x_0) &= \left| \tilde{S}(\tilde{x}_1, x_0) \right|^2 \\ &= \left| a_{-1} \tilde{E}(2\tilde{x}_1) + a_0 \tilde{E}(\tilde{x}_1) + a_1 \tilde{E}(0) + a_3 \tilde{E}(2\tilde{x}_1) \right|^2 \\ &= \left| a_0 \tilde{E}(\tilde{x}_1) + a_1 \tilde{E}(0) \right|^2 \end{aligned} \quad (A.2)$$

$$I_{IR}(\tilde{x}_1, x_0) = \left| \tilde{E}(0) \right|^2 \left| \frac{2}{\pi} \sin\left(\xi \frac{\pi}{2}\right) e^{i(\xi \frac{\pi}{2} - \phi_1)} + \cos\left(\xi \frac{\pi}{2}\right) e^{i\xi \frac{\pi}{2}} \frac{\tilde{E}(\tilde{x}_1)}{\tilde{E}(0)} - \frac{2 \sin\left(\xi \frac{\pi}{2}\right)}{\pi} e^{i(\xi \frac{\pi}{2} + \phi_1)} \frac{\tilde{E}(2\tilde{x}_1)}{\tilde{E}(0)} + \frac{2 \sin\left(\xi \frac{\pi}{2}\right)}{3\pi} \right|^2 \quad (A.3)$$

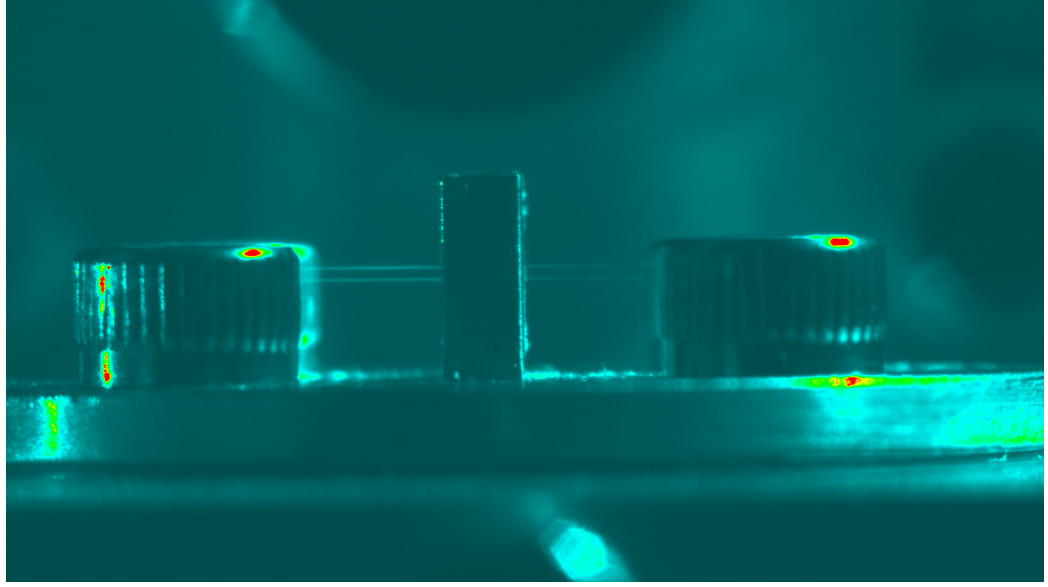


Figure A.1: Camera image of two sources generating a filament in a gas cell. Image was taken while chamber was vented and at ambient pressure.

$$\begin{aligned}
I_{IR}(\tilde{x}_1, x_0) &= \left| \tilde{E}(0) \frac{2}{\pi} \sin\left(\xi \frac{\pi}{2}\right) \right|^2 \left| e^{-i\phi_1} + \frac{\pi}{2 \tan(\xi \frac{\pi}{2})} \frac{\tilde{E}(\tilde{x}_1)}{\tilde{E}(0)} - e^{i\phi_1} \frac{\tilde{E}(2\tilde{x}_1)}{\tilde{E}(0)} + \frac{e^{-3i\phi_1}}{3} \frac{\tilde{E}(2\tilde{x}_1)}{\tilde{E}(0)} \right|^2 \\
&= \left| \tilde{E}(0) \frac{2}{\pi} \sin\left(\xi \frac{\pi}{2}\right) \right|^2 \left( 1 + \frac{\pi}{\tan(\xi \frac{\pi}{2})} \frac{\tilde{E}(\tilde{x}_1)}{\tilde{E}(0)} \cos(\phi_1) - \frac{4}{3} \frac{\tilde{E}(2\tilde{x}_1)}{\tilde{E}(0)} \cos(2\phi_1) \right) \\
I_{IR}(\tilde{x}_{-1}, x_0) &= \left| \tilde{S}(\tilde{x}_{-1}, x_0) \right|^2 \\
&= \left| a_{-1} \tilde{E}(0) + a_0 \tilde{E}(\tilde{x}_1) \right|^2 \\
&= \left| \tilde{E}(0) \right|^2 \left| -\frac{2}{\pi} \sin\left(\xi \frac{\pi}{2}\right) e^{i(\xi \frac{\pi}{2} + \phi_1)} + \cos\left(\xi \frac{\pi}{2}\right) e^{i\xi \frac{\pi}{2}} \frac{\tilde{E}(\tilde{x}_1)}{\tilde{E}(0)} + \frac{2 \sin\left(\xi \frac{\pi}{2}\right)}{\pi} e^{(\xi \frac{\pi}{2} - \phi_1)} \frac{\tilde{E}(2\tilde{x}_1)}{\tilde{E}(0)} - \frac{2 \sin\left(\xi \frac{\pi}{2}\right)}{3\pi} e^{(\xi \frac{\pi}{2} - 3\phi_1)} \frac{\tilde{E}(2\tilde{x}_1)}{\tilde{E}(0)} \right|^2 \\
&= \left| \tilde{E}(0) \frac{2}{\pi} \sin\left(\xi \frac{\pi}{2}\right) \right|^2 \left| e^{-i\phi_1} - \frac{\pi}{2 \tan(\xi \frac{\pi}{2})} \frac{\tilde{E}(\tilde{x}_1)}{\tilde{E}(0)} - e^{i\phi_1} \frac{\tilde{E}(2\tilde{x}_1)}{\tilde{E}(0)} + \frac{e^{-3i\phi_1}}{3} \frac{\tilde{E}(2\tilde{x}_1)}{\tilde{E}(0)} \right|^2 \\
&= \left| \tilde{E}(0) \frac{2}{\pi} \sin\left(\xi \frac{\pi}{2}\right) \right|^2 \left( 1 - \frac{\pi}{\tan(\xi \frac{\pi}{2})} \frac{\tilde{E}(\tilde{x}_1)}{\tilde{E}(0)} \cos(\phi_1) - \frac{4}{3} \frac{\tilde{E}(2\tilde{x}_1)}{\tilde{E}(0)} \cos(2\phi_1) \right) \\
a_0^\xi(x_0) &= \cos\left(\xi \frac{\pi}{2}\right) e^{i\xi \frac{\pi}{2}}
\end{aligned} \tag{A.4}$$

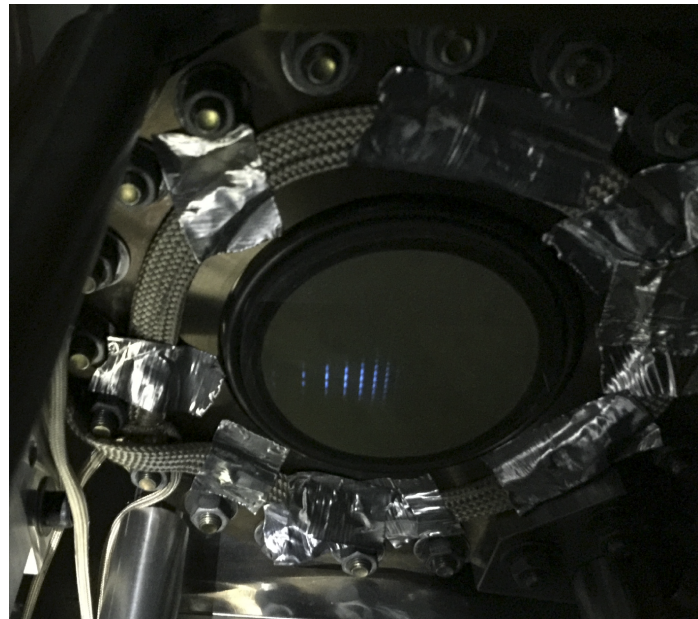


Figure A.2: Camera image of the output of the phosphor screen. Harmonics are visible by eye.

# BIBLIOGRAPHY

- [1] Dietrich Kiesewetter. *Dynamics of Near-Threshold, Attosecond Electron Wavepackets in Strong Laser Fields*. PhD thesis, The Ohio State University, 2019.
- [2] L. A. Romero and F. M. Dickey. Mathematical aspects of laser beam shaping and splitting. In Julie Bentley, Anurag Gupta, and Richard N. Youngworth, editors, *International Optical Design Conference 2010*, page 765225, Jackson Hole, WY, July 2010.
- [3] David T Attwood. *Soft X-Rays and Extreme Ultraviolet Radiation: Principles and Applications*. Cambridge University Press, Cambridge; New York, 2000. OCLC: 818666348.
- [4] U. Fano. Effects of Configuration Interaction on Intensities and Phase Shifts. *Physical Review*, 124(6):1866–1878, December 1961.
- [5] T. Carette, J. M. Dahlström, L. Argenti, and E. Lindroth. Multiconfigurational Hartree-Fock close-coupling ansatz: Application to the argon photoionization cross section and delays. *Physical Review A*, 87(2):023420, February 2013.
- [6] S. L. Wu, Z. P. Zhong, R. F. Feng, S. L. Xing, B. X. Yang, and K. Z. Xu. Electron-impact study in valence and autoionization resonance regions of argon. *Physical Review A*, 51(6):4494–4500, June 1995.
- [7] N. Berrah, B. Langer, J. Bozek, T. W. Gorczyca, O. Hemmers, D. W. Lindle, and O. Toader. Angular-distribution parameters and R-matrix calculations of Ar resonances. *Journal of Physics B: Atomic, Molecular and Optical Physics*, 29(22):5351–5365, November 1996.
- [8] Marieke F. Jager, Christian Ott, Christopher J. Kaplan, Peter M. Kraus, Daniel M. Neumark, and Stephen R. Leone. Attosecond transient absorption instrumentation for thin film materials: Phase transitions, heat dissipation, signal stabilization, timing correction, and rapid sample rotation. *Review of Scientific Instruments*, 89(1):013109, January 2018.

- [9] Marieke Faye Jager. *Attosecond Transient Absorption of Solid-State and Phase-Change Materials*. PhD thesis, University of California, Berkeley, 2017.
- [10] Marie Justine Bell. *Transient Absorption Spectroscopy with Isolated Attosecond Pulses*. PhD thesis, University of California, Berkeley, 2013.
- [11] Chang-Ming Jiang. *Charge Carrier Dynamics in Transition Metal Oxides Studied by Femtosecond Transient Extreme Ultraviolet Absorption Spectroscopy*. PhD thesis, University of California, Berkeley, 2015.
- [12] Lauren Jacqueline Borja. *Electron Dynamics in Solids Studied by Attosecond Extreme Ultraviolet Spectroscopy*. PhD thesis, University of California, Berkeley, 2016.
- [13] Yan Cheng. *Attosecond Transient Absorption Spectroscopy of Atoms and Molecules*. PhD thesis, University of Central Florida, 2015.
- [14] Razvan Cristian Chirla. *Attosecond Pulse Generation and Characterization*. PhD thesis, The Ohio State University, 2011.
- [15] Timothy Thomas Gorman. *Attosecond Probing of Electron Dynamics in Atoms and Molecules Using Tunable Mid-Infrared Drivers*. PhD thesis, The Ohio State University, 2018.
- [16] Frank L. Pedrotti, Leno Matthew Pedrotti, and Leno S. Pedrotti. *Introduction to Optics*. Pearson/Prentice Hall, Upper Saddle River, N.J, 3rd ed edition, 2007.
- [17] Joseph W. Goodman. *Introduction to Fourier Optics*. Roberts & Co, Englewood, Colo, 3rd ed edition, 2005. OCLC: ocm56632414.
- [18] Fred M. Dickey and Scott C. Holswade, editors. *Laser Beam Shaping: Theory and Techniques*. Number 70 in Optical Engineering. Marcel Dekker, New York, 2000.
- [19] Antoine Camper, Hyunwook Park, Stephen J. Hageman, Greg Smith, Thierry Auguste, Pierre Agostini, and Louis F. DiMauro. High relative-phase precision beam duplicator for mid-infrared femtosecond pulses. *Optics Letters*, 44(22):5465–5468, November 2019.
- [20] Louis A. Romero and Fred M. Dickey. Theory of optimal beam splitting by phase gratings I One-dimensional gratings. *Journal of the Optical Society of America A*, 24(8):2280, August 2007.
- [21] Jorge Albero, Jeffrey A. Davis, Don M. Cottrell, Charles E. Granger, Kyle R. McCormick, and Ignacio Moreno. Generalized diffractive optical elements with asymmetric harmonic response and phase control. *Applied Optics*, 52(15):3637, May 2013.

- [22] Louis A. Romero and Fred M. Dickey. The Mathematical Theory of Laser Beam-Splitting Gratings. In *Progress in Optics*, volume 54, pages 319–386. Elsevier, 2010.
- [23] Giacinto Scoles, editor. *Atomic and Molecular Beam Methods*. Oxford University Press, New York, 1988.
- [24] Yasuo Nabekawa, Toshihiko Shimizu, Yusuke Furukawa, Eiji J. Takahashi, and Katsumi Midorikawa. Interferometry of an attosecond pulse train generated from Xe gas target. *Chemical Physics*, 414:20–25, March 2013.
- [25] Y Nabekawa and K Midorikawa. Interferometric autocorrelation of an attosecond pulse train calculated using feasible formulae. *New Journal of Physics*, 10(2):025034, February 2008.
- [26] Yijian Meng, Chunmei Zhang, Claude Marceau, A. Yu. Naumov, P. B. Corkum, and D. M. Villeneuve. Interferometric time delay correction for Fourier transform spectroscopy in the extreme ultraviolet. *Journal of Modern Optics*, 63(17):1661–1667, September 2016.
- [27] M. Kovačev, S. V. Fomichev, E. Priori, Y. Mairesse, H. Merdji, P. Monchicourt, P. Breger, J. Norin, A. Persson, A. L’Huillier, C.-G. Wahlström, B. Carré, and P. Salières. Extreme Ultraviolet Fourier-Transform Spectroscopy with High Order Harmonics. *Physical Review Letters*, 95(22):223903, November 2005.
- [28] I Jong Kim, Chul Min Kim, Hyung Taek Kim, Gae Hwang Lee, Yong Soo Lee, Ju Yun Park, David Jaeyun Cho, and Chang Hee Nam. Highly Efficient High-Harmonic Generation in an Orthogonally Polarized Two-Color Laser Field. *Physical Review Letters*, 94(24):243901, June 2005.
- [29] N. Dudovich, J. L. Tate, Y. Mairesse, D. M. Villeneuve, P. B. Corkum, and M. B. Gaarde. Subcycle spatial mapping of recollision dynamics. *Physical Review A*, 80(1):011806, July 2009.
- [30] N. Dudovich, O. Smirnova, J. Levesque, Y. Mairesse, M. Yu Ivanov, D. M. Villeneuve, and P. B. Corkum. Measuring and controlling the birth of attosecond XUV pulses. *Nature Physics*, 2(11):781–786, November 2006.
- [31] Joachim Stöhr. *NEXAFS Spectroscopy*. Number 25 in Springer Series in Surface Sciences. Springer-Verlag, Berlin ; New York, 1992.
- [32] Christopher J. Kaplan, Peter M. Kraus, Andrew D. Ross, Michael Zürch, Scott K. Cushing, Marieke F. Jager, Hung-Tzu Chang, Eric M. Gullikson, Daniel M. Neumark, and Stephen R. Leone. Femtosecond tracking of carrier relaxation in germanium with extreme ultraviolet transient reflectivity. *Physical Review B*, 97(20):205202, May 2018.

- [33] Anthony Cirri, Jakub Husek, Somnath Biswas, and L. Robert Baker. Achieving Surface Sensitivity in Ultrafast XUV Spectroscopy: M<sub>2,3</sub>-Edge Reflection–Absorption of Transition Metal Oxides. *The Journal of Physical Chemistry C*, 121(29):15861–15869, July 2017.
- [34] B. L. Henke, P. Lee, T. J. Tanaka, R. L. Shimabukuro, and B. K. Fujikawa. Low-energy x-ray interaction coefficients: Photoabsorption, scattering, and reflection: E = 100–2000 eV Z = 1–94. *Atomic Data and Nuclear Data Tables*, 27(1):1–144, January 1982.
- [35] D. Hemmers, M. Benzid, and G. Pretzler. Direct measurement of the complex refractive index of thin foils in the XUV spectral range by point diffraction interferometry. *Applied Physics B*, 108(1):167–175, July 2012.
- [36] D. Hemmers and G. Pretzler. Multi-color XUV interferometry using high-order harmonics. *Applied Physics B*, 95(4):667–674, June 2009.
- [37] Lucy A. Wilson, Andrew K. Rossall, Erik Wagenaars, Cephise M. Cacho, Emma Springate, I. C. Edmond Turcu, and Greg J. Tallents. Double slit interferometry to measure the EUV refractive indices of solids using high harmonics. *Applied Optics*, 51(12):2057–2061, April 2012.
- [38] T. Ditmire, E. T. Gumbrell, R. A. Smith, J. W. G. Tisch, D. D. Meyerhofer, and M. H. R. Hutchinson. Spatial Coherence Measurement of Soft X-Ray Radiation Produced by High Order Harmonic Generation. *Physical Review Letters*, 77(23):4756–4759, December 1996.
- [39] B. L. Henke, E. M. Gullikson, and J. C. Davis. X-Ray Interactions: Photoabsorption, Scattering, Transmission, and Reflection at E = 50-30,000 eV, Z = 1-92. *Atomic Data and Nuclear Data Tables*, 54(2):181–342, July 1993.
- [40] He Wang, Michael Chini, Shouyuan Chen, Chang-Hua Zhang, Feng He, Yan Cheng, Yi Wu, Uwe Thumm, and Zenghu Chang. Attosecond Time-Resolved Autoionization of Argon. *Physical Review Letters*, 105(14):143002, October 2010.
- [41] Christian Reinhold Ott. *Attosecond Multidimensional Interferometry of Single and Two Correlated Electrons in Atoms*. Dissertation, 2012.
- [42] V. Stoop, S. M. Cavaletto, S. Donsa, A. Blättermann, P. Birk, C. H. Keitel, I. Březinová, J. Burgdörfer, C. Ott, and T. Pfeifer. Real-Time Reconstruction of the Strong-Field-Driven Dipole Response. *Physical Review Letters*, 121(17):173005, October 2018.

- [43] Andreas Kaldun, Christian Ott, Alexander Blättermann, Martin Laux, Kristina Meyer, Thomas Ding, Andreas Fischer, and Thomas Pfeifer. Extracting Phase and Amplitude Modifications of Laser-Coupled Fano Resonances. *Physical Review Letters*, 112(10):103001, March 2014.
- [44] A. Kaldun, A. Blättermann, V. Stooß, S. Donsa, H. Wei, R. Pazourek, S. Nagele, C. Ott, C. D. Lin, J. Burgdörfer, and T. Pfeifer. Observing the ultrafast buildup of a Fano resonance in the time domain. *Science*, 354(6313):738–741, November 2016.
- [45] H. Beutler. Über Absorptionsserien von Argon, Krypton und Xenon zu Termen zwischen den beiden Ionisierungsgrenzen  $2P_{3/2}/0$  und  $2P_{1/2}/0$ . *Zeitschrift für Physik*, 93(3):177–196, March 1935.
- [46] Ugo Fano. Sullo spettro di assorbimento dei gas nobili presso il limite dello spettro d’arco. *Il Nuovo Cimento (1924-1942)*, 12(3):154–161, March 1935.
- [47] Herman Feshbach. Unified theory of nuclear reactions. *Annals of Physics*, 5(4):357–390, December 1958.
- [48] Herman Feshbach. A unified theory of nuclear reactions. II. *Annals of Physics*, 19(2):287–313, August 1962.
- [49] A. K. Bhatia and A. Temkin. Line-shape parameters for  $\hat{^1}P$  Feshbach resonances in He and  $\hat{^1}\mathrm{Li}^+$ . *Physical Review A*, 29(4):1895–1900, April 1984.
- [50] Andrey E. Miroshnichenko, Sergej Flach, and Yuri S. Kivshar. Fano resonances in nanoscale structures. *Reviews of Modern Physics*, 82(3):2257–2298, August 2010.
- [51] Zenghu Chang. *Fundamentals of Attosecond Optics*. CRC Press, Boca Raton, 2011.
- [52] W.-C. Chu and C. D. Lin. Theory of ultrafast autoionization dynamics of Fano resonances. *Physical Review A*, 82(5):053415, November 2010.
- [53] C. Ott, A. Kaldun, P. Raith, K. Meyer, M. Laux, J. Evers, C. H. Keitel, C. H. Greene, and T. Pfeifer. Lorentz Meets Fano in Spectral Line Shapes: A Universal Phase and Its Laser Control. *Science*, 340(6133):716–720, May 2013.
- [54] Christian Ott, Andreas Kaldun, Luca Argenti, Philipp Raith, Kristina Meyer, Martin Laux, Yizhu Zhang, Alexander Blättermann, Steffen Hagstotz, Thomas Ding, Robert Heck, Javier Madroñero, Fernando Martín, and Thomas Pfeifer. Reconstruction and control of a time-dependent two-electron wave packet. *Nature*, 516(7531):374–378, December 2014.
- [55] Andreas Kaldun. *Fano Resonances in the Time Domain - Understanding and Controlling the Absorption and Emission of Light*. PhD thesis, 2014.